Steel-Plate Composite Wall to Reinforced Concrete Wall Mechanical Connection—Part 2: In-Plane and Out-Of-Plane Shear Strength

Hassan S. Anwar, Jungil Seo, Amit H. Varma, and Yoonho Nam

ABSTRACT

In safety-related nuclear facilities, steel-plate composite (SC) walls are often used in combination with reinforced concrete (RC) walls or foundations. The design demands need to be transferred between the two different structural systems through appropriate connection design. A design procedure was developed by the authors, and it was evaluated by conducting two full scale tests for SC wall-to-RC wall mechanical connections subjected to out-of-plane flexure. The experimental and numerical results are discussed in Part 1 (Seo et al., 2022). This paper presents a brief description of the design procedure as well as the experimental and numerical investigations conducted to further evaluate the design procedure. The focus was on the performance, strength, and governing failure mode of an SC wall-to-RC wall mechanical connection under in-plane and out-of-plane shear. The investigation results include global force-displacement and applied force-strain responses. The paper also presents overall damage progression in terms of concrete cracking patterns. The experimentally observed and numerically predicted results indicate that the proposed connection design procedure is suitable and conservative for SC wall-to-RC wall mechanical connections.

Keywords: Reinforced concrete, steel-plate composite, mechanical connection, full-strength connection design, wing plate, tie plate, baseplate, In-plane shear, out-of-plane shear, LS-DYNA

INTRODUCTION

Steel-plate composite (SC) walls forming a modular construction system have emerged as a viable alternative to conventional reinforced concrete (RC) walls over the past decade. A typical SC wall is comprised of two steel faceplates, concrete infill, steel headed stud anchors, and tie bars as illustrated in Figure 1. This innovative structural wall has well-known benefits, including superb structural performance (Ozaki et al., 2004; Varma et al., 2014; Bruhl et al., 2015a; Sener et al., 2015; Anvari et al., 2020), and construction schedule economy (DOE, 2006; IAEA, 2011). Consequently, SC walls are continuously gaining interest in the commercial building industry as well as in nuclear power plant construction. In the building industry, SC walls are being used as primary lateral load-resisting systems in high-rise construction. In safety related nuclear facilities, SC walls are being used in lieu of conventional RC walls in the construction of AP1000® in the United States and China as well as in the design of US-APWR®. SC walls are designed to withstand seismic, wind, impulse, impact, and accident thermal loadings (Sener and Varma, 2021), and they typically replace RC walls to prevent rebar congestion due to higher force demands (Seo and Varma, 2017a). However, it is challenging to completely replace RC walls with SC walls in a structure for multiple reasons such as: (i) lack of code provisions for structural systems that are not governed by AISC N690, *Specification for Safety-Related Steel Structures for Nuclear Facilities* (AISC, 2018), (ii) costs associated with implementing SC walls in the entire structure, and (iii) the designer's personal preference for RC walls. Thus, their potential for superior structural performance and accelerated construction schedules can only be realized through appropriate connections between SC walls and RC walls.

SC-to-RC connections can be categorized as: (i) SC wall-to-RC wall connections, (ii) SC wall-to-RC slab connections, and (iii) SC wall-to-RC basemat connections. SC-to-RC connections can be difficult to design as the structural behavior and force transfer mechanisms of the two systems are different from each other. In addition, different connecting elements such as post-tensioned reinforcement, steel headed stud anchors, and shear lugs, etc. (Bhardwaj and Varma, 2017) can be considered for transferring different in-plane and out-of-plane design demands.

Hassan S. Anwar, Graduate Research Assistant, Purdue University, West Lafayette, Ind. Email: hsagheer@purdue.edu (corresponding)

Jungil Seo, Research Assistant Professor, Purdue University, West Lafayette, Ind. Email: seo2@purdue.edu

Amit H. Varma, Karl H. Kettelhut Professor and Director of Bowen Laboratory, Purdue University, West Lafayette, Ind. Email: ahvarma@purdue.edu

Yoonho Nam, Engineering Group Supervisor, Civil & Architectural Engineering Dept. KEPCO E&C, Korea, Email: yoonho.nam@gmail.com

Paper No. 2022-02

JEAC (2009) recommends three connection techniques to transfer forces between an SC wall and an RC basemat, namely, (a) embedding steel faceplates in the RC basemat via shear connectors, (b) anchoring the steel faceplates and RC basemat dowel bars to the baseplate, and (c) non-contact lap splicing between faceplates and dowel bars. These techniques are discussed by Seo et at. (2022).

The SC wall can be connected to an RC wall using a non-contact lap splice or mechanical connections. Typically, more than one reinforcement layer is used in RC walls due to higher force demands. A non-contact lap splice connection for rebar larger than 1.4 in. diameter (#11) would require significant development length (L_d) which may not be an option at certain locations. To prevent this issue, mechanical splicing of rebar greater than 1.4 in. diameter (#11) can be done using the guidance provided by ACI 349-06, *Code Requirements for Nuclear Safety-Related Concrete Structures and Commentary* (ACI, 2006). However, design requirements for mechanical splicing of reinforcement (#11 and beyond) in RC structures per ACI 349-06 cannot be easily applied to SC wall-to-RC wall mechanical connections. This is attributed to the involved force transfer mechanisms associated with two different structural systems and lack of prescriptive design requirements in AISC N690. Therefore, a design procedure for the SC wall-to-RC wall mechanical connection was developed by the authors based on available design philosophy and concepts.

This paper focuses on the behavior and design of only SC wall-to-RC wall mechanical connections, as the other two connections have already been explored by Kurt (2016) and Seo and Varma (2017b). It presents: (i) a brief description of the development of the design procedure, (ii) results and observations from both experimental and numerical investigations conducted to evaluate the performance of the designed mechanical connection under in-plane shear (IPV) and out-of-plane shear (OOPV), and (iii) validation of the design procedure.

BACKGROUND

SC-RC structural connections can be designed in accordance with the performance-based connection design philosophies permitted by AISC N690 for SC wall connections. Accordingly, the design procedure can be based on either an overstrength connection philosophy or a full-strength connection philosophy. In the case of an overstrength connection, the connection is designed for 200% of seismic and 100% of the nonseismic design demands. However, the connection can be weaker than the connected structures. When a full-strength connection is implemented, the connection is designed to develop the full strength (125%) of the weaker of the connected structural members. That is, the energy dissipation in the formation of a plastic hinge would occur outside the connection region during a design basis or beyond seismic event. For this reason, the full-strength connection design is preferred in most cases.

The IPV and OOPV need to be transferred from the concrete and steel components of the RC wall to the SC wall and vice versa. Therefore, it is important to develop a basic understanding of the response of the SC wall under such loading scenarios before discussing the different SC wall-to-RC connection techniques. The behavior of an RC wall under such loading is well known (Biskinis et al., 2004; Mo et al., 2008; Carrillo et al., 2013; Usta, 2017), and will not be repeated here.

In-Plane Shear (IPV) Behavior of SC Wall

The IPV response of SC wall panels was experimentally investigated by Ozaki et al. (2004). The testing program consisted of nine square specimens of 47.2 × 47.2 × 7.9 in. size as shown in Figure 2. The test specimens were subjected to cyclic IPV. The study investigated the influence of steel plate thickness, axial force, and partitioning the web. The specimens exhibited good ductility with a linear relationship between yield strength and steel-plate thickness. The findings from Ozaki et al. (2004) were used to

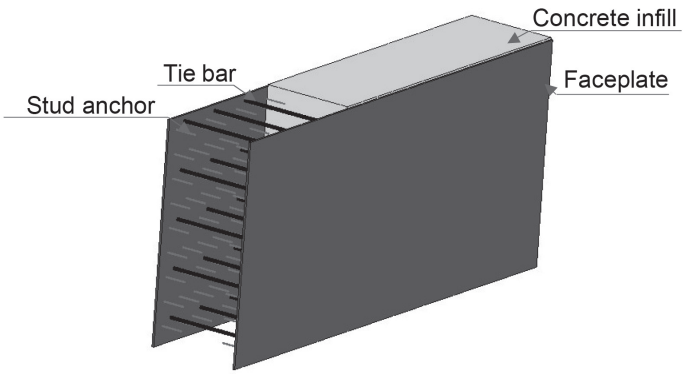

Fig. 1. Typical layout of SC wall.

develop a tri-linear response based on a mechanics based model (MBM) by Varma et al. (2014). The SC wall in-plane (IP) behavior can be simplified into a linear response in three stages: (i) concrete pre-cracking stage where concrete and steel components are in elastic range, (ii) concrete post-cracking stage where steel components are still in elastic range, and (iii) von Mises yield stage with no additional strength or stiffness. The study by Varma et al. (2014) concluded that the MBM model was conservative in predicting the response of SC wall panels tested by Ozaki et al. (2004).

An experimental study was conducted by Epackachi et al. (2015a) to investigate the influence of wall thickness, reinforcement ratio, and tie bar and shear connector spacing on the IP cyclic behavior of rectangular SC walls. The four SC wall specimens, anchored to the concrete basemat using a baseplate bolted connection, failed in flexure. The study concluded that the distance between shear connectors and the baseplate had significant impact on the post-peak shear behavior.

Seo et al. (2016) compiled a comprehensive experimental database of the 26 tests conducted on SC walls (with boundary elements) in the US, Japan, and South Korea. The experimentally observed IPV strength from these tests was compared with the strength predicted by the MBM, ACI 349-06 (ACI, 2006), and AISC N690s1, Specification for Safety-Related Steel Structures for Nuclear Facilities Including Supplement No. 1, (AISC, 2015) design code equations. It was concluded that the design equations used in AISC N690s1 and the MBM predicted the shear strength conservatively, and that the faceplate reinforcement ratio is the key parameter influencing the IPV strength.

Booth et al. (2020) developed an analytical approach using composite shell theory to determine IP response of the SC walls. Equations for predicting the ultimate shear strength and peak shear stains were developed and verified using an existing experimental database of the SC walls. The authors reported that existing shear strength estimation, based on the von Mises yielding of faceplates, is a lower bound estimate because it does not include post-yield shear strength of the walls.

Out-of-Plane Shear (OOPV) Behavior of SC Wall

Sener and Varma (2021) carried out an experimental and analytical study to evaluate the OOPV behavior of SC walls. The test matrix included 10 full-scale SC walls with design parameters including section depth, shear and longitudinal reinforcement ratios, shear span-to-depth ratio, and faceplate thickness. A typical configuration of the full-scale SC wall from the test matrix is shown in Figure 3. The results of this study concluded that current AISC N690 design recommendations are adequate for estimating OOPV strength of SC walls.

SC-RC Connections

Seo and Varma (2017a) experimentally investigated the axial behavior of non-contact lap splice connections, which is one of the typical connection techniques between an SC wall and RC basemat (connection type "c" discussed in the introduction). The authors identified the force transfer mechanism of the connection and developed design recommendations for the SC-to-RC non-contact lap splice connections based on experimental and numerical results.

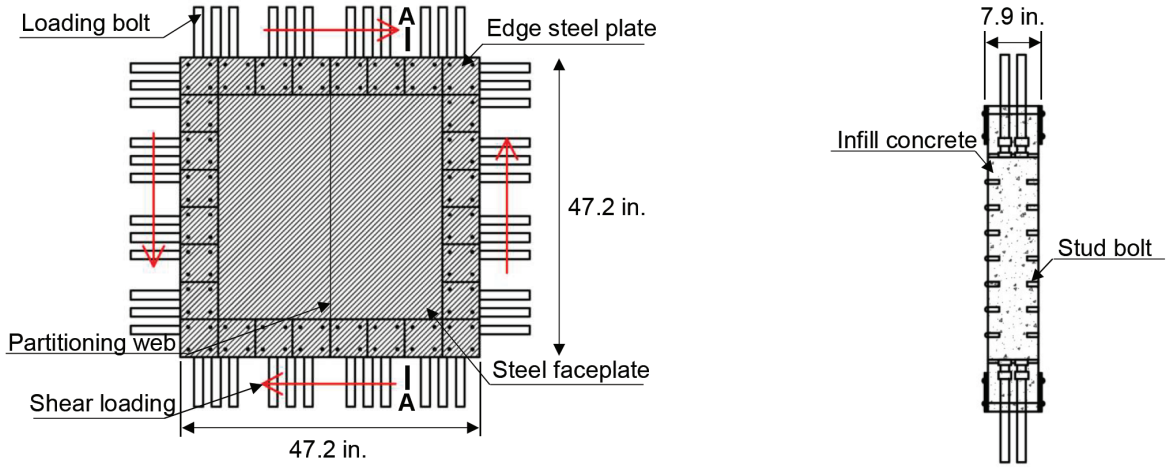

(a) Plan View *(b) Section view A-A*

Fig. 2. SC wall panel in-plane shear test (Ozaki et al., 2004).

Kurt (2016) investigated the full-strength connection philosophy by conducting an experimental and numerical study. SC wall specimens with aspect ratios (h_{wall}/l_{wall}) ranging from 0.6 to 1 were subjected to cyclic in-plane shear until failure. Details of the full-strength connection between the SC wall and RC foundation are shown in Figure 4. The results of this investigation were used to propose design equations to predict the lateral loading capacity of SC walls. The study concluded that the IPV strength decreased with an increase in the aspect ratio of the SC walls.

Seo et al. (2022) developed the design procedure for mechanical connections between SC and RC walls using the full-strength connection design philosophy. Experimental and numerical studies were conducted to evaluate the performance of the mechanical connection designed under out-of-plane flexure. The study concluded that the proposed design procedure was suitable and conservative for designing SC wall-to-RC wall mechanical connections. It was recommended that additional investigations need to be conducted to verify the performance of the design procedure for different loading conditions.

FORCE TRANSFER MECHANISM AND DESIGN PROCEDURE

Figure 5 illustrates the main force transfer mechanism of the SC wall-to-RC wall connection subjected to IPV and OOPV. The shear force transfer takes place across the two concrete surfaces (SC and RC) through friction as a result of clamping force in the rebar embedded in both the SC and RC walls. In this study, it was assumed that the mechanical connection can develop 125% of the yield strength of each rebar, $T_1 = T_2 = T_3 = T_4 = 1.25A_{s,r}F_{y,r}$. That is, sufficient embedment length is provided to the rebar in the RC portion, and therefore, no premature failure of the RC portion associated with the rebar embedment length occurs.

The assumption also results in the maximum shear friction force, V_nSF, of $1.25A_{s,r}F_{y,r}$ per rebar. However, the shear friction force is limited by the lesser of $(480+0.08f_c')A_c$, $0.2f_c'A_c$, and $1600A_c$ in accordance with ACI 318-19, *Building Code Requirements for Structural Concrete* (ACI, 2019), Section 22.9.4.4, where A_c is the area of concrete parallel to the applied shear. In addition, the shear strength of the RC portion (with conventional shear reinforcement)

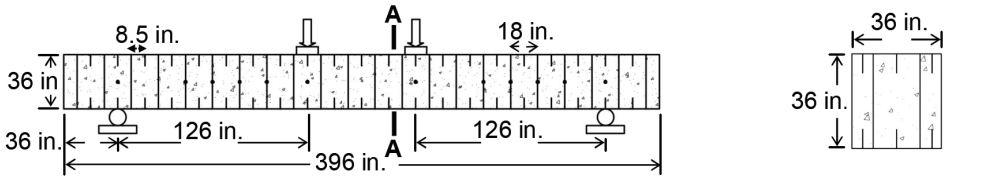

(a) Elevation view *(b) Section view A-A*

Fig. 3. SC wall four-point bending test (Sener and Varma, 2021).

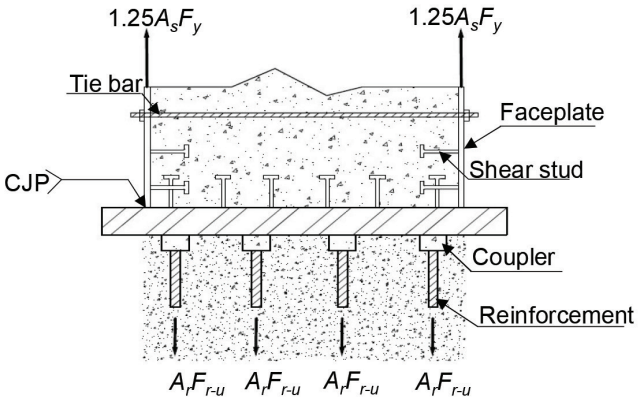

Fig. 4. Full-strength connection between SC wall and concrete foundation (Kurt, 2016).

is less than that of the SC portion. This would potentially result in the shear failure of the RC portion prior to the SC portion while developing rebar strength less than 125% of the rebar yield strength. Additionally, the axial force from the rebar is transferred to the faceplates, which generates eccentric moment that is resisted by SC infill concrete near the baseplates and tie plates that connect the two faceplates.

Additional assumptions made for the design procedure include (1) connected RC and SC walls have already been designed with the same thickness and (2) the wing plate and baseplate have the same width. Figure 6 shows a typical configuration of the designed SC wall-to-RC wall mechanical connection. As shown, the RC wall flexural reinforcement is extended inside the SC wall and connected to the baseplates using mechanical couplers. Baseplates are welded to faceplates and wing plates to provide stability against rebar forces. Tie plates, welded to the faceplates, are provided to resist the tensile component of the moment generated due to eccentricity.

Tie Plate Design

Figure 7 illustrates how the rebar force induced by transferring shear force through shear friction is transferred to the mechanical connection region. In the figure, $R_{u,tp}$ is the required axial force involved in the design of the tie

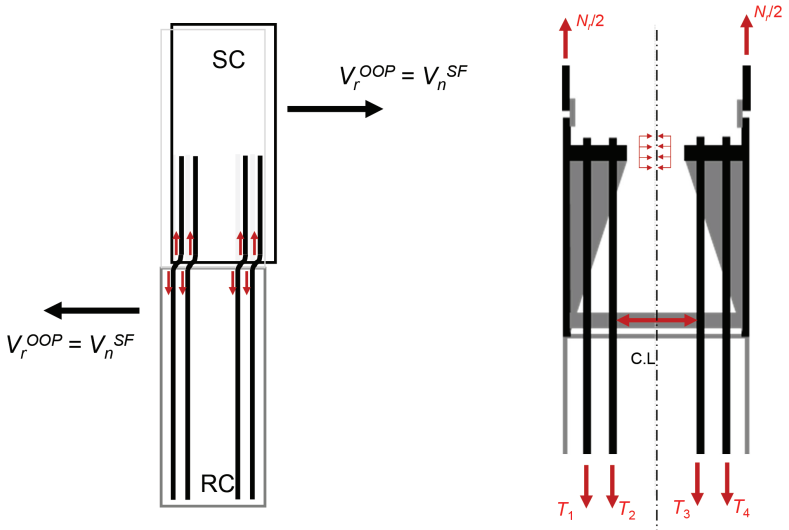

Fig. 5. IPV and OOPV force transfer mechanism (Seo et al., 2022).

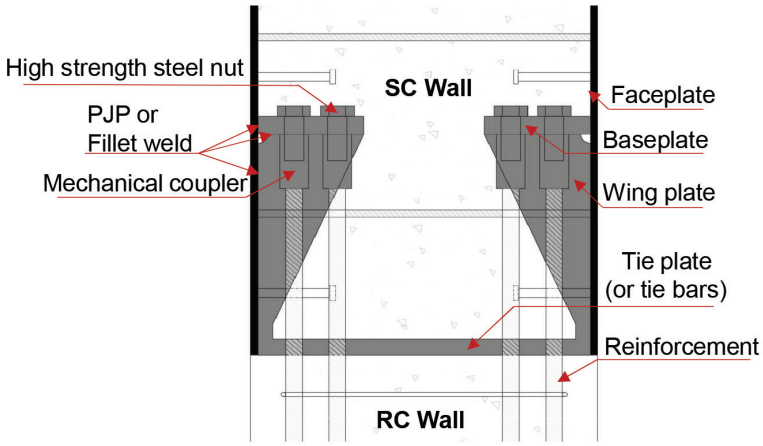

Fig. 6. Typical configuration of mechanical splice connection (Seo et al., 2022).

plate. As shown, the magnitude of $R_{u,tp}$ can be determined by taking the moment about 'O' and the resulting equation is shown as Equation 1. In the equation, h_3 and h_4 are the respective rebar distances from the centerline (CL), h_{tp} is the center-to-center distance between the tie plate and the baseplate, t_p is the faceplate thickness, t_{wall} is the thickness of the wall, and N_r is the maximum transferrable axial force from RC wall-to-SC wall.

$$R_{u,tp} = \frac{\left[\frac{N_r}{2}\left(\frac{t_{wall}}{2} - \frac{t_p}{2}\right)\right] - (T_3 h_3 + T_4 h_4)}{h_{tp}} \quad (1)$$

Baseplate Design

Baseplate design is performed for a unit length of 1 in. using the yield line method. The unit length of the baseplate is subjected to two concentrated forces from the steel reinforcement equal to 125% of the yield strength per rebar ($1.25A_{s,r}F_{y,r}$). The yield line method considers the structural element at its collapse state. The details of the collapse mechanism and respective yield lines corresponding to the flexural capacities (M^+, M^-) are shown in Figure 8. W_{bp} is the width of baseplate, whereas $t_{p,wp}$ and S_{wp} are the thickness and spacing between the wing plates, respectively. Additionally, S_{r1} is the distance of the rebar from the faceplate and S_{r2} is the center-to-center distance between the rebar. Figure 9 illustrates the external work ($\sum W_{ext}$) done in undergoing small deflection (Δ) and the internal work ($\sum W_{int}$) done in rotations (θ_1, θ_2) along yield lines. The required flexural capacity of the baseplate ($M_{u,bp}$) can be determined by equating $\sum W_{ext}$ and $\sum W_{int}$, where $\sum$Wext, $\sum W_{int}$, and $M_{u,bp}$, are given by Equations 2, 3, and 4, respectively.

$$\sum W_{ext} = 2P\Delta = 2(1.25A_{s,r}F_{y,r})\Delta \quad (2)$$

$$\sum W_{int} = \sum Ml\theta \quad (3)$$

$$M_{u,bp} = M = \frac{2(1.25A_{s,r}F_{y,r})\Delta}{2l_1\theta_1 + l_2(\theta_1+\theta_2) + l_3(\theta_1+\theta_2) + l_4\theta_1 + l_6\theta_1 + l_5\theta_2} \quad (4)$$

where

$\Delta = 1$

$l_1 = W_{bp} - S_{r1} - 1.5d_{hole}$

$l_2 = l_3 = \sqrt{\left(\frac{S_{wp} - t_{p,wp}}{2}\right)^2 + (S_{r1})^2} - \frac{1}{2}d_{hole}$

$l_4 = l_6 = W_{bp}$

$l_5 = S_{wp} - t_{p,wp}$

Finally, the minimum baseplate thickness, $t_{p,bp,min}$, can be computed from the ratio of required strength to available design strength ($\phi M_{n,bp} = \phi F_y Z$) as shown in Equation 5:

$$t_{p,bp,min} = \sqrt{\frac{8(1.25A_{s,r}F_{y,r})}{\frac{2l_1\theta_1 + l_2(\theta_1+\theta_2) + l_3(\theta_1+\theta_2) + l_4\theta_1 + l_6\theta_1 + l_5\theta_2}{\phi F_{y,bp}}}} \quad (5)$$

where

$$Z = \frac{(1\text{ in.})(t_{p,bp})^2}{4}$$

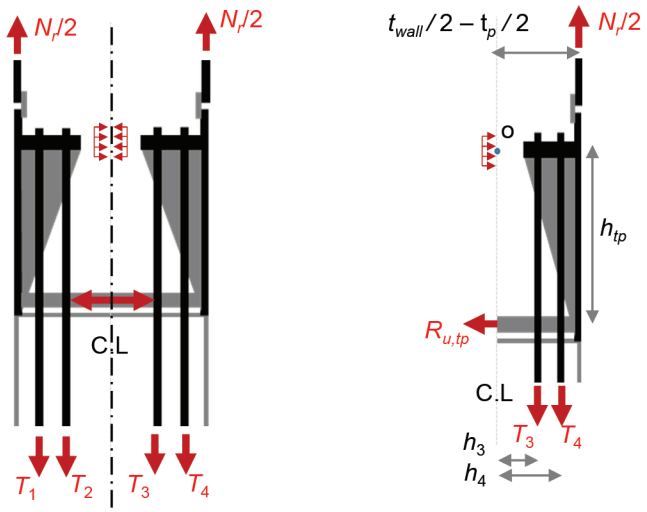

Fig. 7. Required axial force ($R_{u,tp}$) for tie plate design (Seo et al., 2022).

Wing plate Design

The geometry and loading conditions of the wing plate shown in Figure 10 are identical to the triangular bracket seat as shown in the Companion to the AISC Steel Construction Manual Volume 1 (AISC, 2019). Thus, the triangular bracket seat design can be implemented for the wing plate if *P*, *a*, and *b* [Figure 10(b)] can be replaced by T_1+T_2, htp, and Wbp [Figure 10(a)]. The design process involves determination of the wing-plate thickness and calculation of demands and available strengths along section A-A and B-B as shown in Figure 10(b).

EXPERIMENTAL PROGRAM

The experimental investigations were conducted to evaluate the performance of the SC wall-to-RC wall mechanical connections designed through the procedure already shown. The experimental program involved testing seven mechanical connections comprised of four full-scale and three scaled specimens. Full-scale specimens were subjected to monotonic out-of-plane moment (OOPM) and OOPV, whereas the scaled specimens underwent cyclic IPV. In the current study, only OOPV (2 full scale) and IPV (2 small scale) loading scenarios are discussed. One scaled specimen exhibited significant voids and honeycombing during concrete casting, therefore useful experimental data could not be obtained from that specimen. The remaining 2 large-scale specimens subjected to OOPM are presented in Seo et al. (2022).

Design of Test Matrix

The test matrix was designed keeping in mind typical settings of a safety related nuclear facility. Test setup of specimens subjected to OOPV is shown in Figure 11. As shown, the specimen had a wall thickness, T_{wall}, of 36 in. and a wall width, w_{wall}, of 18 in. The length of the test unit, l_{span}, was

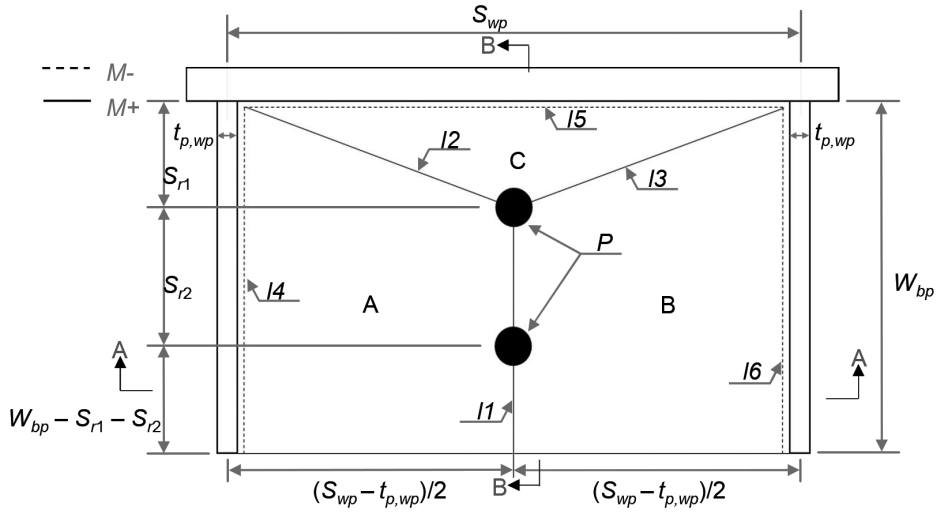

Fig. 8. Yield line method for baseplate design (Seo et al., 2022).

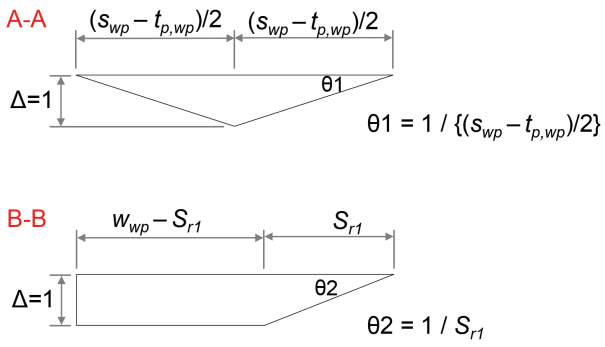

Fig. 9. Small deflection and rotations at section A-A and B-B (Seo et al., 2022).

180 in. ($5.0T_{wall}$). The SC wall portion is comprised of ¾ in. Gr. 50 faceplates (t_p), a reinforcement ratio (ρ_2) of 0.04, 1-in.-diameter steel headed stud anchors at 9 in. center-to-center spacing (s_s), and ASTM A706 Grade 60 #8 tie bars (connecting the faceplates with partial-joint-penetration welds) at 18 in. center-to-center spacing (s_t). The RC wall portion consisted of ASTM A706 Gr. 60 #14 flexural reinforcement (d_b = 1.69 in.) at center-to-center spacing ($s_{1,rc}$) of 9 in. with a longitudinal reinforcement ratio (ρ_1) of 0.014. The longitudinal rebar were placed in four curtains as a pair along each edge. Shear reinforcement of ASTM A706 Gr. 60 #4 double hoop stirrups were placed at the same center-to-center

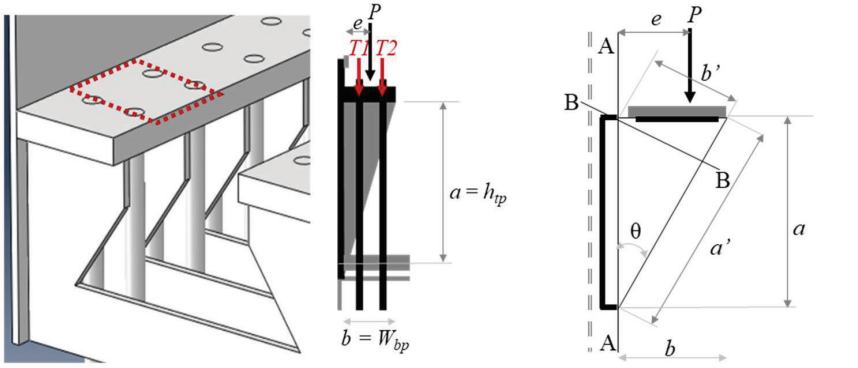

(a) Wing plate *(b) Bracket seat per AISC (2019)*

Fig. 10. Geometry and loading comparison (Seo et al., 2022).

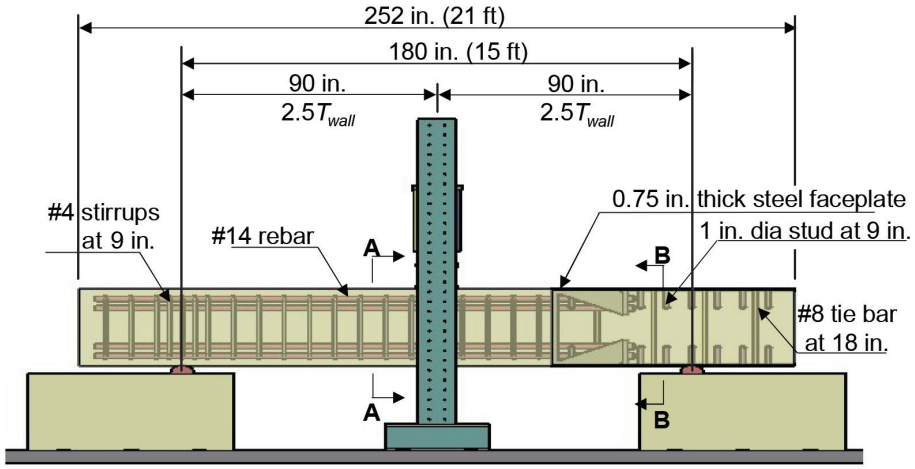

(a) Elevation view

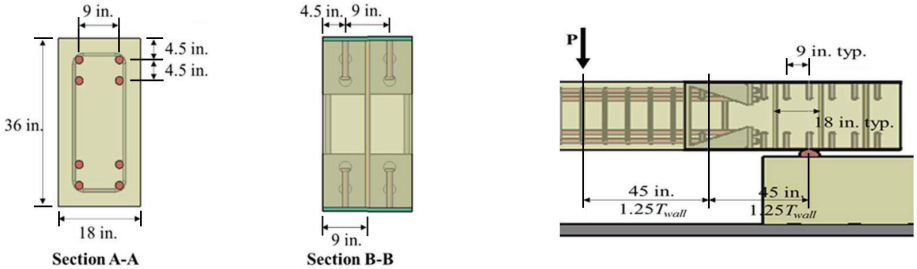

(b) Section view A-A *(c) Section view B-B* *(d) Connection region*

Fig. 11. OOPV test specimen.

spacing (9 in.) along the length of the RC wall. The connection region was comprised of a 1.75-in.-wide (w_{tp}) and 1-in.-thick tie plate (t_{tp}), an 11-in.-wide (w_{bp}) × 2-in.-thick baseplate (t_{bp}), and a 1-in.-thick wing plate (t_{wp}). The connection region was 27 in. long, and all steel plates within the mechanical connection region were Gr. 50.

The test setup of specimens subjected to IPV is shown in Figure 12. The ratio between full scale specimens (OOPV) and reduced scale specimens (IPV) was selected to be 1:3. Hence, the thickness (T_{wall}) and length of wall (l_{span}) for IPV specimens were 12 in. and 60 in., respectively. The specimen height-to-length ratio (h_{wall}/l_{span}) was kept to 1 to maximize the shear contribution. The 1:3 scaling refers to the geometric scaling of the RC and SC portions. However, the exact scaling could not be achieved for the longitudinal rebar. Consequently, the mechanical connection region was redesigned based on the developed design procedure. The SC wall portion consisted of ¼-in.-thick ASTM Gr. 50 faceplates (t_p), a reinforcement ratio (ρ_2) of 0.04, ¼-in.-diameter steel headed stud anchors at center-to-center spacing (s_s) of 3 in., and ASTM A706 Gr. 60 #4 tie bars at center-to-center spacing (s_t) of 6 in. The RC wall portion was comprised of ASTM A706 Gr. 60 #5 longitudinal and horizontal reinforcement (d_b = 0.62 in.), at center-to-center spacing ($s_{1,rc}$) of 3 in., with a reinforcement ratio (ρ_1) of 0.034. The connection region was 9 in. long and comprised of Gr. 50 steel plates constituting a 0.625-in.-wide (w_{tp}) × ⅜-in.-thick tie plate (t_{tp}), a 3.75-in.-wide (w_{bp}) × ⅝-in.-thick baseplate (t_{bp}), and a ⅜-in.-thick wing plate (t_{wp}).

The details of the test matrix are summarized in Table 1. The 2 full-scale and 2 scaled specimens mentioned in Table 1 are nearly identical to each other; the only difference is the rebar-to-baseplate connection configuration. Figure 13 illustrates the two connection plans considered in this study. The coupler (C) connection configuration utilizes a coupler to connect the tapered threaded longitudinal rebar to the baseplate using a high strength bolt (ASTM A449) as shown in Figure 13(a). The double nut (DN) connection configuration also utilizes the coupler, which is connected to the tapered threaded longitudinal rebar at one end and a threaded rod at the other end. The threaded rod is secured to the baseplate utilizing double nuts as shown in Figure 13(b). Table 2 presents the average measured material properties of the test specimens. The concrete strength represents the average measured strength at the day of test as per ASTM C39 (ASTM, 2014) standards. The table also shows the steel uniaxial tensile strength measured according to the ASTM E8 (ASTM, 2013) standards. The yield stress, F_y, was measured according to the 0.2% offset rule.

Instrumentation and Loading Protocol

The test setup of OOPV specimens subjected to monotonic loading, with a 500-kip hydraulic actuator at 45 in. away from the center of the connection region is shown in Figure 11. The arrangement of string potentiometers (SP) and displacement transducers (DT) is presented in Figure 14. As shown, SP1 was attached to the center of the connection region, and a pair of SP2/SP3 was attached under the loading point to measure global deflection and possible twisting of the test setup. Lastly, SP4 was attached under the center of the RC wall portion. One set of two DT was

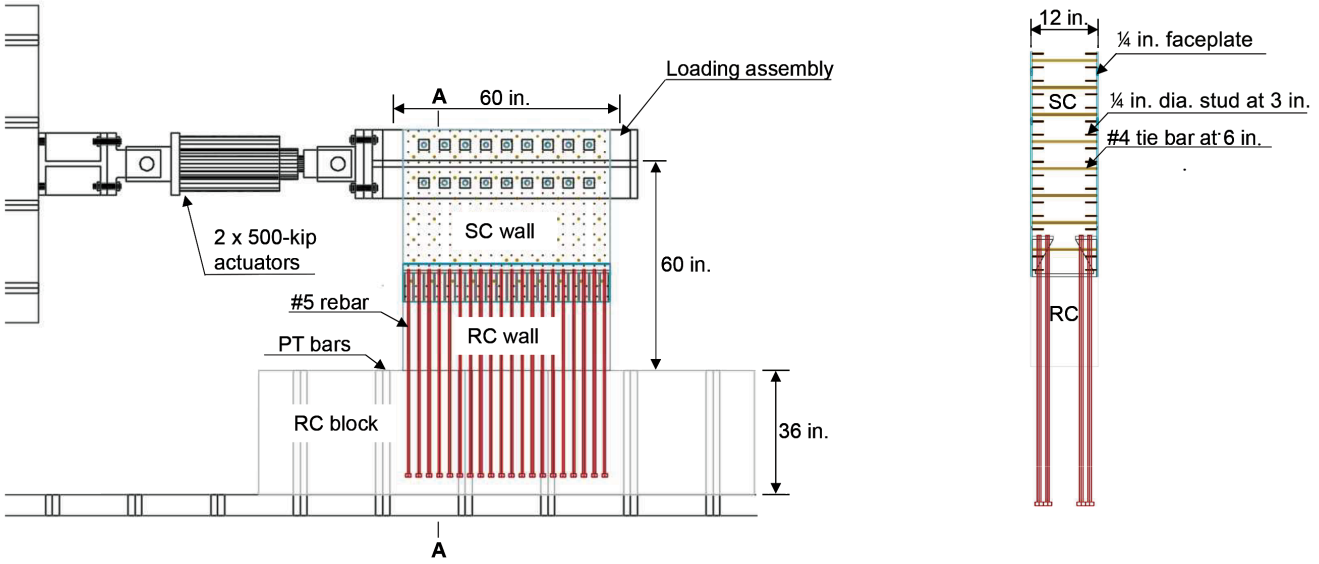

(a) Elevation view *(b) Section view A-A*

Fig. 12. IPV test specimen.

Table 1. Geometric Details of the Test Matrix															
	Overall Dimension			SC Wall				RC Wall			Connection				
Specimen	w_{wall}, h_{wall} (in.)	l_{span} (in.)	T_{wall} (in.)	t_p (in.)	ρ_2	s_s (in.)	s_t (in.)	d_b (in.)	$s_{1,rc}$ (in.)	ρ_1	w_{tp} (in.)	t_{tp} (in.)	w_{bp} (in.)	t_{bp} (in.)	t_{wp} (in.)
OOPV-C	18	180	36	¾	0.04	9	18	1.69	9	0.014	1.75	1	11	2	1
OOPV-DN	18	180	36	¼	0.04	9	18	1.69	9	0.014	1.75	1	11	2	1
IPV-C	60	60	12	¼	0.04	3	6	0.62	3	0.034	0.625	⅜	3.75	⅝	⅜
IPV-DN	60	60	12	¼	0.04	3	6	0.62	3	0.034	0.625	⅜	3.75	⅝	⅜

Table 2. Measured Properties of Test Specimens								
	Steel Yield Strength, F_y (ksi)						Concrete Strength, f'_c (ksi)	Connection Plan
Specimen	Faceplate	Baseplate	Tie Plate	Wing plate	Rebar	Stirrup		
OOPV-C	59	62	57	57	68	67	5.81	Coupler
OOPV-DN	59	62	57	57	68	67	5.76	Double nut
IPV-C	63	63	60	63	65	—	5.93	Coupler
IPV-DN	63	63	60	63	65	—	5.43	Double nut

placed under each roller support to measure the possibility of support settlement. Figure 15 shows the configuration of four electrical-resistance strain gauges (SG) on the interior wing plate and tie plate. One set of two SG was attached on the top and bottom of the baseplates using the configuration shown in Figure 16. In the case of #14 horizontal reinforcement, a pair of SG were attached on each rebar at a horizontal distance of 2 in. from the mechanical coupler as shown in Figure 17. Additionally, one set of two SG was attached on each alternate longitudinal rebar in the RC wall portion under the loading point as shown in Figure 18. Six pairs of SG were also installed on the shear stirrups near the loading point as per Figure 19. The overall lateral behavior of the actual structure is governed by the IPV behavior of both SC and RC walls, which serve as the primary lateral load-resisting system. Therefore, the IPV test specimens were subjected to cyclic lateral loading. The RC portion of the specimens was cast monolithically with the RC block. The RC block was post-tensioned to the laboratory strong floor to prevent sliding and overturning. The post-tensioning forces were designed to prevent any decompression of the concrete foundation from the strong floor, thus providing fixed base conditions. Lateral cyclic loading (and displacement) was applied using two 500-kip hydraulic actuators attached to the laboratory reaction wall and the loading assembly. The test setup of IPV specimens is shown in Figure 12. The lateral loading was increased cyclically as shown in Figure 20. In the figure, V_n is the lateral loading corresponding to the RC wall shear strength calculated using ACI 349-06 (ACI, 2006) Section 21.7.4.1. The measured material properties were used in the calculation, Δ_y is the projected displacement at V_n. Because the test specimens were expected to fail in a non-ductile manner, the displacement at the first cycle of $0.75V_n$ was used to calculate Δ_y. The displacement

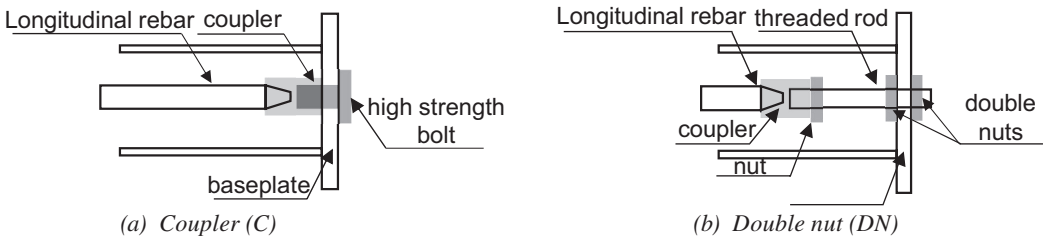

(a) Coupler (C) *(b) Double nut (DN)*

Fig. 13. Rebar to baseplate connection configuration (Seo et al., 2022).

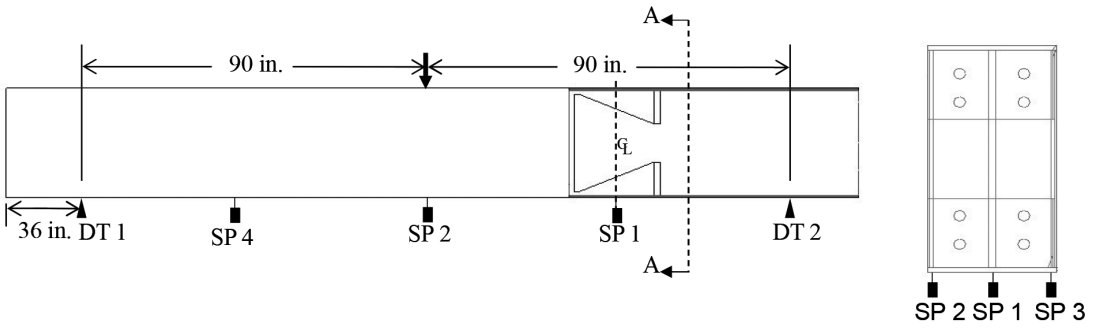

(a) Elevation view *(b) Section view A-A*

Fig. 14. SP and DT sensor layout (OOPV).

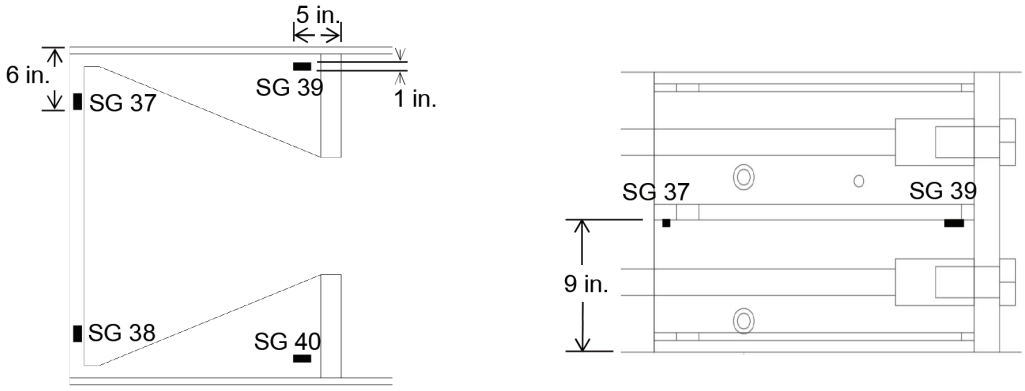

(a) Elevation view *(b) Plan view*

Fig. 15. SG layout of wing plates and tie plates (OOPV).

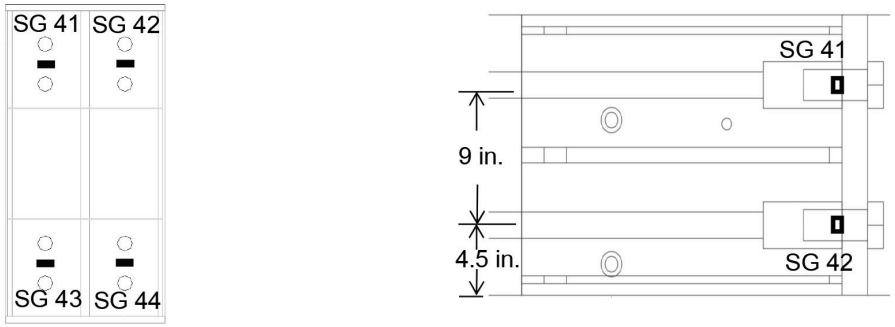

(a) Elevation view *(b) Plan view*

Fig. 16. SG layout of baseplates (OOPV).

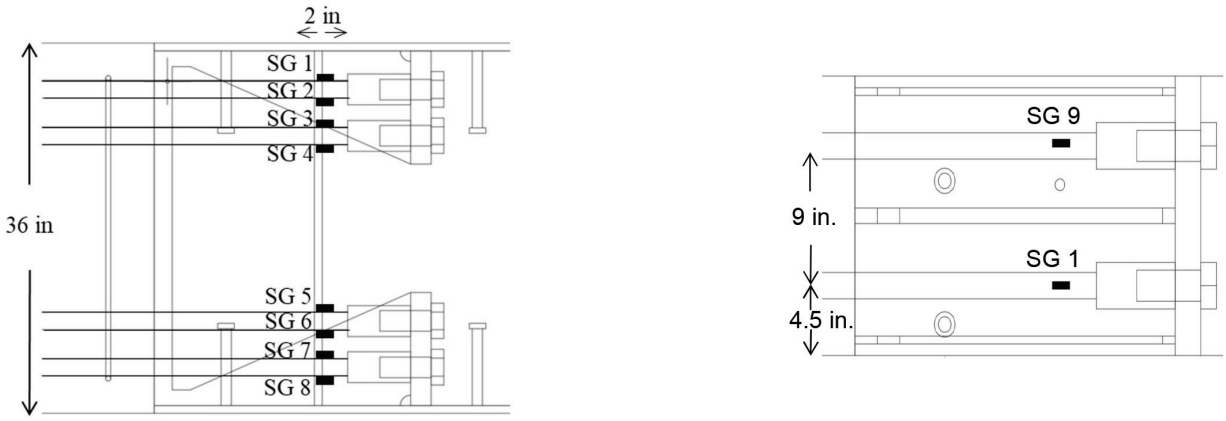

(a) Elevation view *(b) Plan view*

Fig. 17. SG layout of #14 rebar (OOPV).

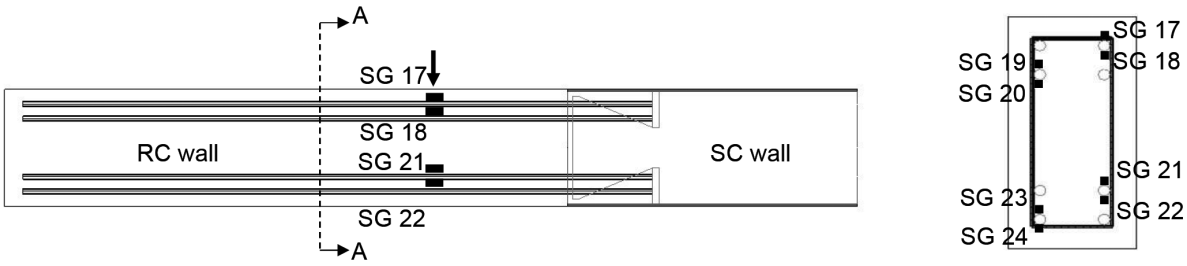

(a) Elevation view *(b) Section view A-A*

Fig. 18. SG layout of #14 rebar at loading point (OOPV).

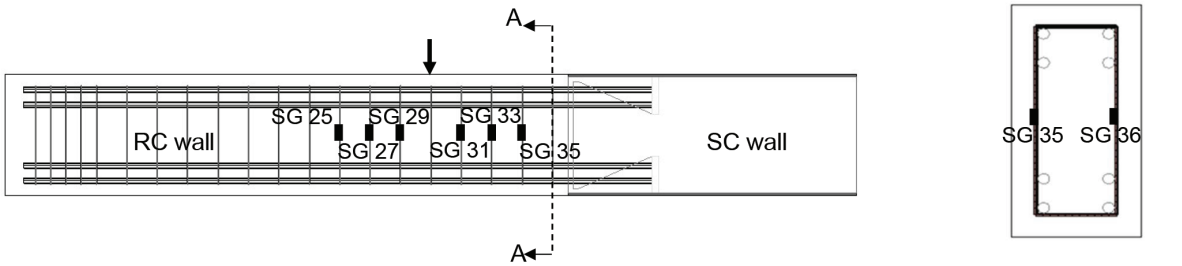

(a) Elevation view *(b) Section view A-A*

Fig. 19. SG layout of stirrups (OOPV).

at $0.75V_n$ was multiplied by 1.33 to estimate Δ_y. Additional displacement cycles with different amplitudes ($1.5\Delta_y$, $2.0\Delta_y$, and $3.0\Delta_y$) were also included in the loading protocol.

A total of seven SPs were utilized to measure the displacement of the RC wall, connection region, SC wall, and foundation block as shown in Figure 21. SP1-SP4 were employed to obtain lateral displacement profiles of the test setup by obtaining values at the loading point and the middle of the SC wall, connection region, and RC wall, respectively. SP5 was used to measure any base slip of the RC wall portion that may have occurred during the test. Lastly, SP6 and SP7 were used to measure vertical displacements. Strain gauge configuration on the tie plates was similar to the OOPV test specimens. Two SG each on exterior tie plate and wing plate were installed on each face of the wall as illustrated in Figure 22. Four pairs of SG were mounted on the vertical rebar at the base of the RC wall on each end (north and south), located at a horizontal distance of 4 in. from the RC foundation block as illustrated in Figure 23. Thus, a total of sixteen SG were installed on the specimen vertical rebar.

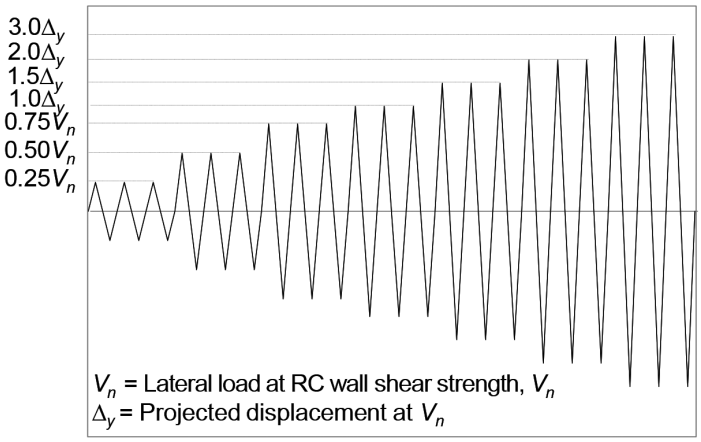

Fig. 20. IPV test loading protocol.

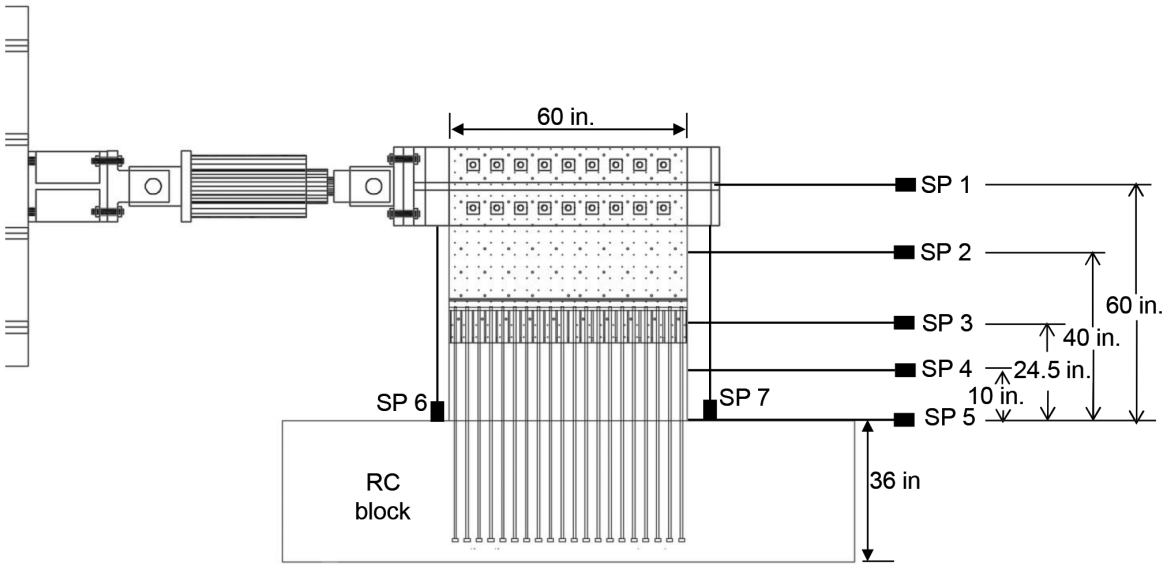

Fig. 21. SP layout (IPV).

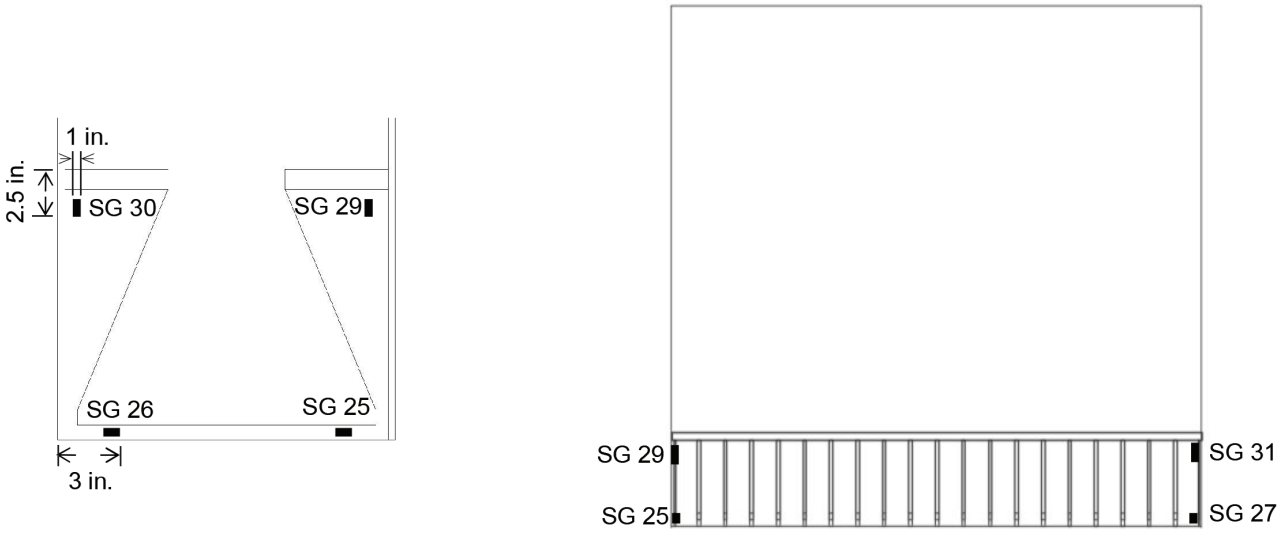

(a) Side view *(b) Elevation view*

Fig. 22. SG layout of wing plates and tie plates (IPV).

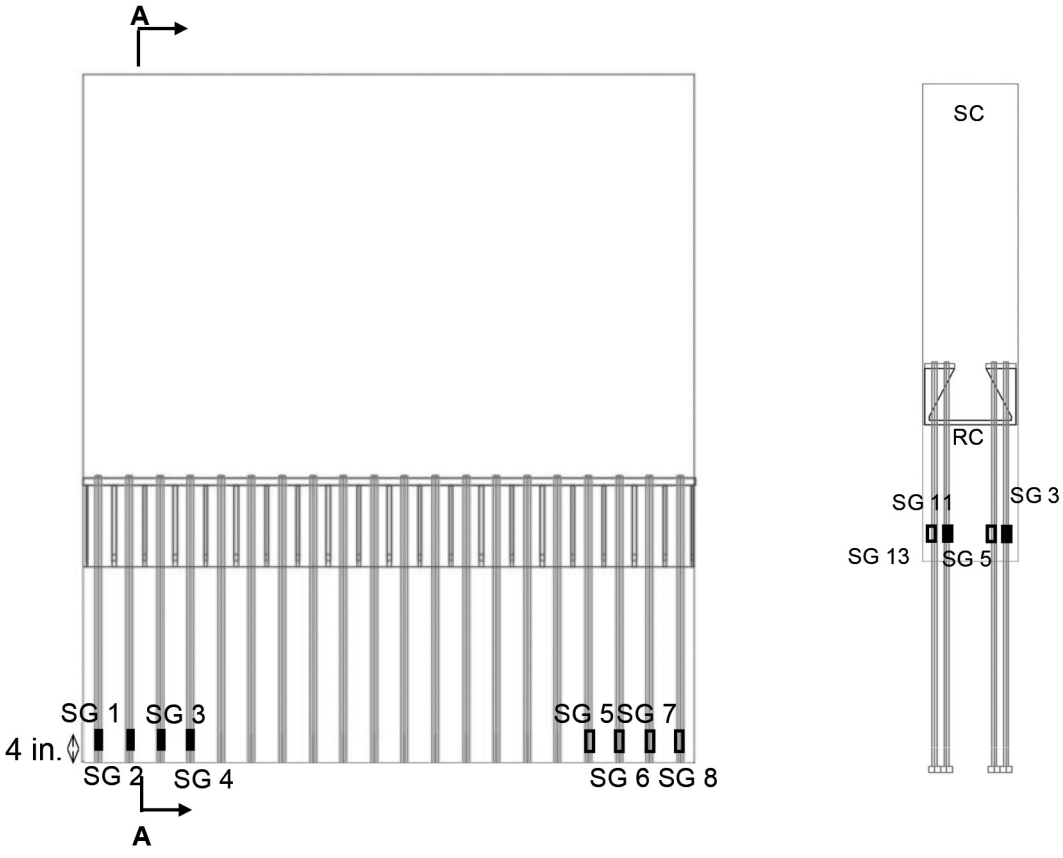

(a) Elevation view *(b) Section view A-A*

Fig. 23. SG layout of #5 rebar (IPV).

EXPERIMENTAL RESULTS

Specimen OOPV-C

Figure 24 shows the overall response in terms of the applied shear—displacement curves. The experimentally measured maximum shear force, V_{max}, was 205 kips, and the corresponding vertical displacements were 0.72 in., 0.41 in., and 0.38 in. at the center, at the RC wall portion, and at the SC wall portion respectively. As shown, initial concrete flexural cracks occurred in the RC wall portion at the applied shear, V, of 50 kips, resulting in changes in the stiffness. Additionally, a rapid increase in the displacement at V_{max} was observed in the RC wall portion due to significant cracking followed by yielding of the shear stirrups. As expected, the maximum displacement, Δ_{max}, was observed under the loading point (SP2,3). V_{max} was greater than the shear capacity of the RC wall portion calculated using ACI 349-06 using measured properties ($V_{n.RC}$ = 167 kips) by 38 kips (22%). The shear force associated with the flexural capacity of the RC wall portion ($V_{Mn.RC}$ = 174 kips) was greater than $V_{n.RC}$ confirming RC shear failure as the governing failure mode.

Figure 25 shows the applied shear–strain response for #14 rebar, #4 stirrups, tie plate, and baseplate. As shown, the bottom #14 rebar under the loading point exhibited strains greater than yield strain (ε_y = 2,328 με) with a maximum strain value of 2,555 με (SG 22). The maximum strain measured from the SG attached next to the couplers was 1,000 με (SG 16). Cracking in the RC wall portion is reflected in the form of yielding of the shear reinforcement with a maximum strain of 2,828 με (SG 25) at V_{max}. Additionally, the maximum strain for the tie plate and baseplate at V_{max} was 1,370 με (SG 38, tie plate) and 436 με (SG 44, baseplate) respectively, with corresponding stress values of

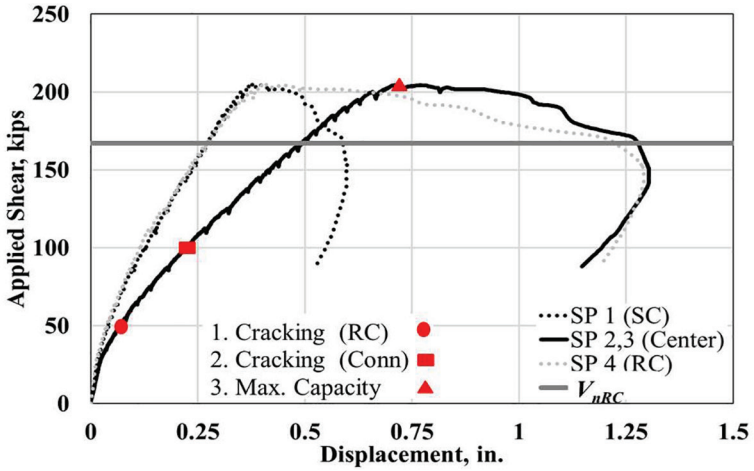

Fig. 24. Applied shear–displacement response (OOPV-C).

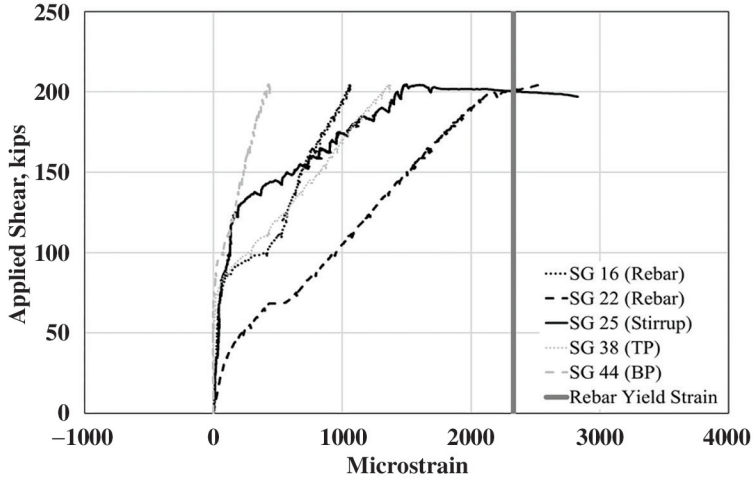

Fig. 25. Applied shear–strain response—#14 rebar, #4 stirrups, tie plate, and baseplate (OOPV-C).

39.7 ksi and 12.6 ksi. Thus, indicating conservatism in the design connection procedure.

Figure 26 shows the overall damage progression in terms of concrete crack patterns. Initially, flexural cracks occurred at the bottom of the RC wall portion at about 24% of V_{max}. As the load increased to 36% of V_{max}, the flexural cracks transformed into flexural-shear cracks along with the formation of new cracks within the RC wall portion. The first shear crack occurred in the connection region at around 100 kips ($0.5V_{max}$). Ultimately, the specimen failed as these diagonal tension cracks (shear cracks) connected the loading point and RC wall portion support as shown in the figure.

Specimen OOPV-DN

The applied shear–displacement response of Specimen OOPV-DN is shown in Figure 27. As shown, the response is similar to that observed from OOPV-C. The experimentally measured maximum shear, V_{max}, was 189 kips, and the corresponding vertical displacements were 0.99 in., 0.68 in., and 0.47 in. at the center, at the RC wall portion, and the SC wall portion, respectively. Initial concrete flexural cracks occurred in the RC wall portion at the applied shear, V, of 50 kips. Additionally, a rapid increase in the displacement at V_{max} was observed in the RC wall portion due to significant cracking followed by yielding of the shear stirrups. As expected, Δ_{max} was observed under the loading point (SP2,3). V_{max} was greater than the RC shear capacity calculated based on ACI 349-06 provisions using measured properties ($V_{n.RC}$ = 167 kips) by 13%. The shear force associated with the flexural capacity of the RC wall portion ($V_{Mn.RC}$ = 174 kips) was greater than $V_{n.RC}$. Thus, confirming RC shear failure as the governing failure mode.

Figure 28 presents the applied shear–strain response for #14 rebar, #4 stirrups, tie plate, and baseplate. As shown, the bottom #14 rebar under the loading point exhibited strains greater than yield strain (ε_y = 2,328 με) with a maximum strain value of 2,873 με (SG 24), whereas the maximum strain value of the rebar next to the couplers was approximately 1,000 με (SG 7). Cracking in the RC wall portion resulted in yielding of the shear reinforcement exhibiting a maximum strain of 2,622 με (SG 26) at V_{max}. Lastly, the respective maximum strain values for the tie plate and baseplate at V_{max} were 1,012 με (SG 37) and 245 με (SG 43) with corresponding stresses of 29.3 ksi and 7.10 ksi. Thus, the

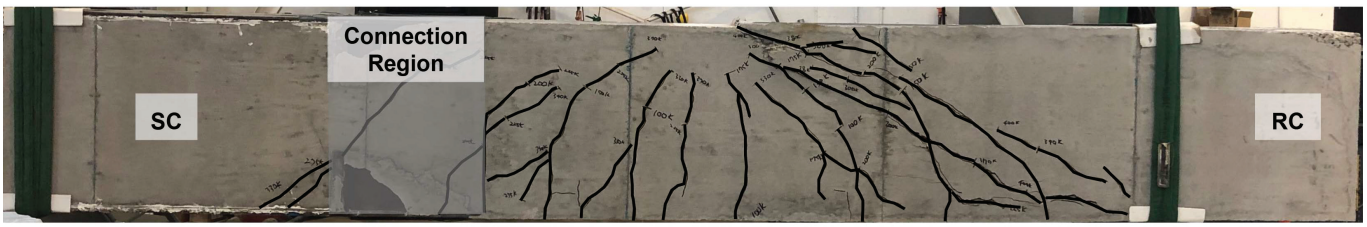

Fig. 26. Concrete crack pattern (west side) (OOPV-C).

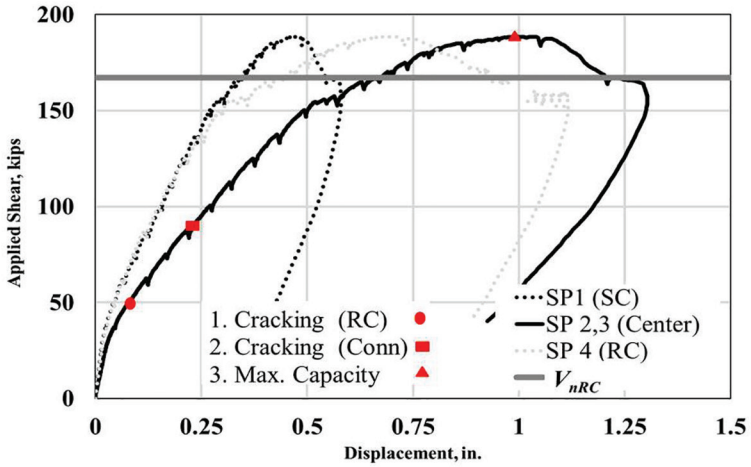

Fig. 27. Applied shear-displacement response (OOPV-DN).

steel components of the connection region remained well within the elastic range.

The overall damage progression in terms of concrete crack patterns is again similar to OOPV-C as shown in Figure 29. Initially, flexural cracks occurred in the bottom of the RC wall portion near the loading point at $0.26V_{max}$. These cracks transformed into flexural-shear cracks along with the formation of additional cracks within the RC wall portion. Shear cracks appeared in the connection region at around 90 kips. Ultimately, the specimen failed due to inelastic diagonal cracks that connected the loading point and RC wall portion support.

Specimen IPV-C

Figure 30 shows the applied force-displacement response of Specimen IPV-C. The response was developed using the measured displacement from SP1. As shown, the specimen behaved in an elastic manner during the first six cycles ($0.25H_n$ and $0.50H_n$). During the first $0.75H_n$ cycle, #5 rebar located at the far south side of the specimen started yielding. During the first $1.5\Delta_y$ cycle, the specimen reached the maximum load, $V_{max.push}$, of 582 kips in push and 576 kips ($V_{max.pull}$) in pull, resulting in the average maximum load, V_{max}, of 579 kips. The corresponding lateral displacements were 0.59 in. (push) and 0.66 in. (pull). The concrete at the

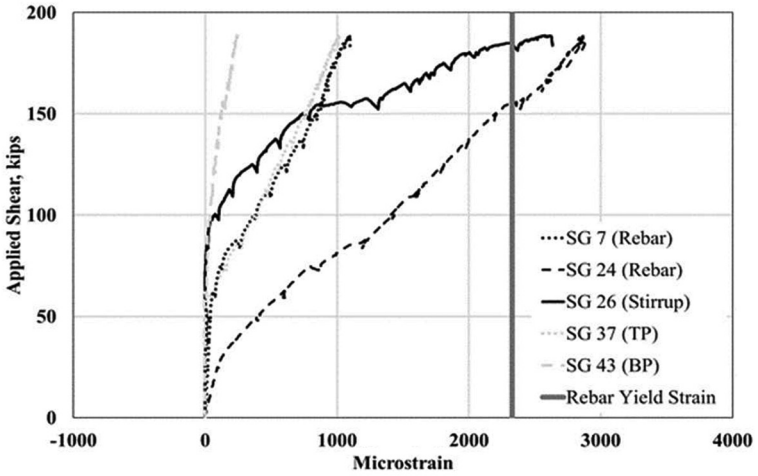

Fig. 28. Applied shear-strain response—#14 rebar, #4 stirrups, tie plate, and baseplate (OOPV-DN).

Fig. 29. Concrete crack pattern (east side) (OOPV-DN).

north toe of the RC wall portion started crushing just before V_{max}. V_{max} is greater than the shear capacity of the RC wall portion ($10f_c'^{0.5}A_c$ = 554 kips) calculated using ACI 349-06 with measured material properties by 25 kips (5%). The load carrying capacity started decreasing due to extensive concrete cracks in the RC wall portion. The specimen failed during the second $2.0\Delta_y$ cycle (push) due to large shear cracks inducing shear failure mode.

Figure 31 shows the applied force–strain response of #5 rebar, tie plates, and wing plates. As shown, the #5 rebar started yielding during the first $0.75H_n$ cycle. The response collected during the first $1.5\Delta_y$ cycle shows that the exterior tie plate (SG 26) almost reached its yield strength exhibiting the maximum strain of 1,932 microstrain (corresponding to 56.0 ksi). The figure also shows the response of wing plates. As presented, it appears that the exterior wingplate (SG 31) exhibited the maximum strain of only –365 microstrain (corresponding to –10.6 ksi). The overall damage progression in terms of concrete crack patterns is shown in Figure 32. Initially, flexural concrete cracks appeared from both ends of the specimen. The RC flexural cracks transformed into flexural-shear cracks, and additional shear cracks were formed during subsequent loading cycles. Eventually, the specimen failed in shear as major shear cracks occurred in the middle of the specimen.

Specimen IPV-DN

Figure 33 shows the overall applied force-displacement behavior of Specimen IPV-DN. As shown, the response was very similar to the specimen tested with the coupler connection plan (IPV-C). The specimen remained in the elastic range during the initial six cycles ($0.25H_n$ and $0.50H_n$). During the first $0.75H_n$ cycle, #5 rebar located at the far south side of the specimen started yielding. During the first $1.5\Delta_y$

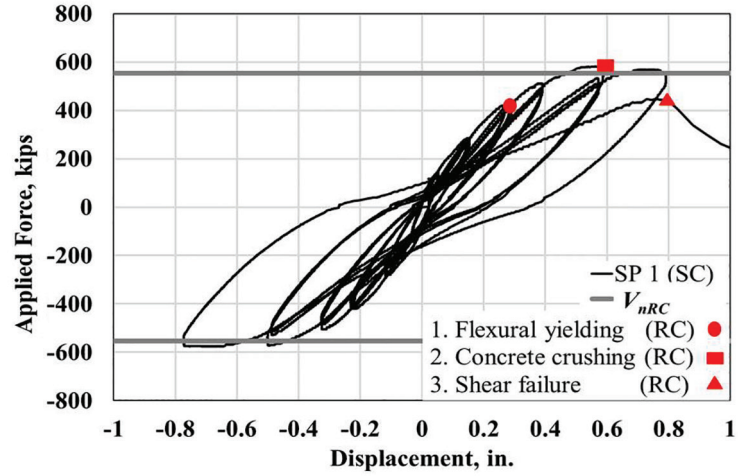

Fig. 30. Applied force-displacement response (IPV-C).

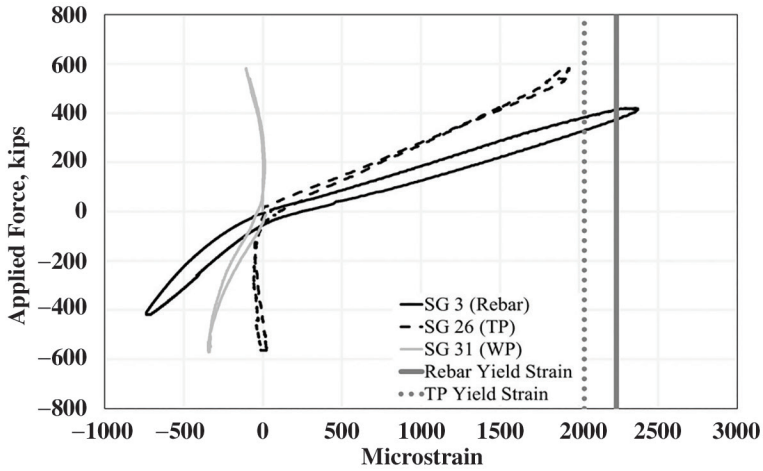

Fig. 31. Applied force-strain response—$0.75H_n$ and $1.5\Delta_y$ (first cycles) (IPV-C).

(a) Elevation view RC wall portion

(b) Side view RC wall portion

Fig. 32. RC wall failure—concrete cracking and spalling (IPV-C).

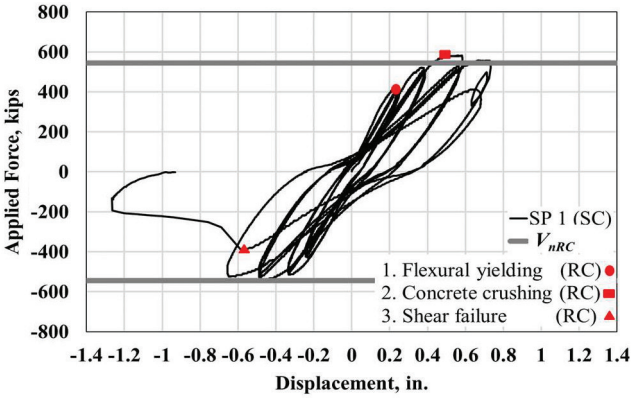

Fig. 33. Applied force-displacement response (IPV-DN).

cycle, the specimen reached the maximum load, $V_{max.push}$, of 582 kips in push and 550 kips in pull, resulting in the average maximum load, V_{max}, of 566 kips. The corresponding lateral displacements were 0.57 in. (push) and 0.46 in. (pull). V_{max} is greater than the shear capacity of the RC wall portion ($10f_c'^{0.5}A_c$ = 531 kips) calculated using ACI 349-06 with measured material properties by 35 kips (or 6%). The concrete at the base of the RC wall portion started crushing just before V_{max}. The load-carrying capacity decreased after V_{max} due to inelastic concrete cracks in the RC wall portion. Ultimately, the specimen failed in shear during the second $2.0\Delta_y$ cycle (pull).

Figure 34 shows the applied force–strain response of #5 rebar and tie plates. As presented, the #5 rebar started yielding during the first $0.75H_n$ cycle. The response collected during the first $1.0\Delta_y$ cycle shows that the exterior tie plate (SG 25) reached its yield strength exhibiting the maximum strain of 2,193 microstrain (63.6 ksi). Figure 35 shows the concrete crack pattern after $2.0\Delta_y$ cycle. As shown, flexural concrete cracks appeared initially from both ends of the specimen, exhibiting a flat (horizontal) crack angle. As the loading increased, additional cracks were formed with inclined crack angles. Eventually, the specimen failed in shear as major cracks occurred in the middle of the specimen.

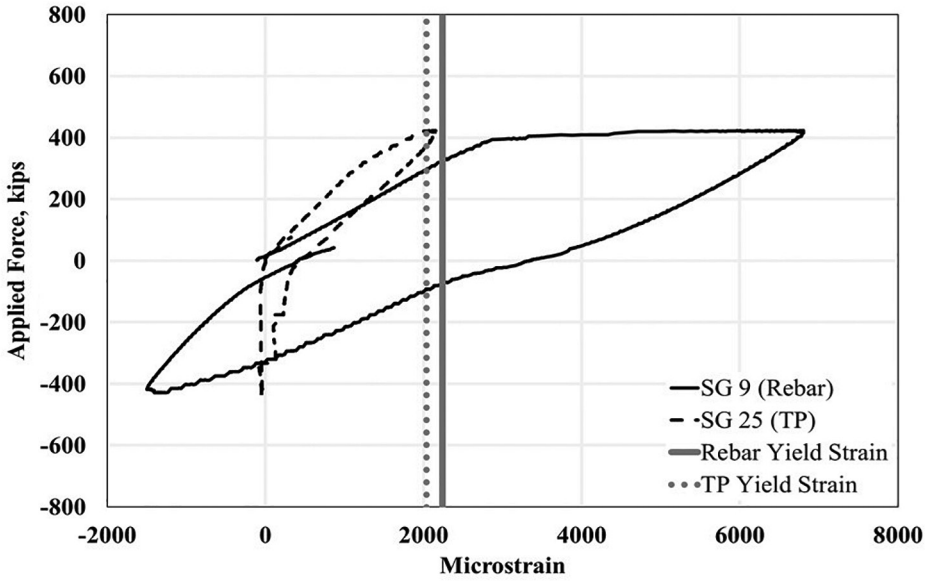

Fig. 34. Applied force strain response—0.75Hn and 1.0Δ_y (first cycles) (IPV-DN).

(a) East side *(b) North side*

Fig. 35. RC wall damage progression (IPV-DN).

FINITE ELEMENT ANALYSES

This section presents the details of three-dimensional (3-D) finite element models (FEMs) developed using LS-DYNA explicit solver (LS-DYNA, 2012a, 2012b). The developed models explicitly accounted for the geometric and material nonlinearities. Numerical analyses were conducted to gain an additional insight into the performance and efficacy of the designed mechanical connection. Details related to the analysis approach, material models, input parameters, and numerical verification of the test results are discussed in the following sections.

Modeling Approach

Numerical models for simulations were created replicating the exact specimen design details covered in the experimental program. SC wall faceplates, tie plates, wing plates, and baseplates of the connection region, and RC wall flexural reinforcement were modeled with 1 in. mesh size solid elements employing full integration element formulation (ELFORM -1). The respective concrete regions of SC and RC walls were also modeled with 1 in. solid elements, however, employing a constant stress reduced integration formulation (ELFORM 1) (LS-DYNA, 2012a, b). The rationale for both these integration techniques used for solid elements in LS-DYNA has been discussed in Part 1 of Seo et al. (2022), and therefore will not be repeated here. Hughes-Liu beam element formulation (1 in. mesh size) with cross-section integration (ELFORM 1) was used to model the RC wall shear reinforcement, SC wall shear connectors, and tie bars. Additionally, other researchers including Bruhl et al. (2015b) and Epackachi et al. (2015b) have also recommended these solid and beam element formulations.

RC wall reinforcement, SC wall shear connectors and tie bars, and the connection region were constrained in respective concrete portions using Constrained_Lagrange_In_Solid (CLIS) keyword depicting a perfect bond. Interaction at the interface between faceplate and infill SC wall concrete, RC wall and SC wall respective concrete portions, and RC wall and foundation concrete (IPV model) were defined via Automatic_Surface_To_Surface contact formulation. This two-way general contact algorithm protects the slave and master nodes against penetration. Additionally, the length of the RC wall vertical rebar extending inside the connection region was less than the development length as per ACI 349 (ACI, 2006), therefore, the same contact definition was used to define their interaction with SC wall infill concrete. Details of LS-DYNA 3D models for OOPV and IPV specimens are presented in Figure 36 and Figure 37.

Material Models and Properties

Material models for simulations were chosen from the library of LS-DYNA (LS-DYNA, 2012a, 2012b). Winfrith_Concrete (MAT 84) and Continuous_Surface_Cap_Model (CSCM) concrete (MAT 159) material models were utilized for simulating IPV and OOPV tests, respectively. The smeared cracking constituent material model (MAT 84) can capture the critical cyclic IPV behavior of concrete such as shear force transfer across cracks due to aggregate interlock, opening and closing of cracks, loss of strength and stiffness parallel to cracks, and tension stiffening, etc. (Teh Hu and Schnobrich; 1990, Vecchio and DeRoo, 1995; Epackachi et al., 2015b). It assumes an elastic perfectly plastic response in compression with plasticity portion based on shear failure surface proposed by Ottosen (1977). The post-cracking behavior of the material model in the tensile region can be simulated using Wittmann's fictitious crack model (Schwer, 2011) based on fracture energy. The fracture energy, G_f, is defined as energy dissipated per unit area during crack opening, and it is equal to the area under the tensile stress-crack width curve. The linear relationship between tensile stress and crack width is considered in this study. Crack width, ω, can be estimated from Equations 6 and 7 (Wittmann et al., 1988), where f_t is the uniaxial tensile strength and Φ is the maximum aggregate size.

$$\omega = \frac{2G_f}{f_t} \tag{6}$$

$$G_f = 1.297\Phi^{0.32} \tag{7}$$

The CSCM concrete material model was developed by the U.S Department of Transportation to predict the performance of concrete involved in roadside safety structures. It is an isotropic model that requires only basic strength data in the form of concrete strength, f'_c, and aggregate size. The cardinal difference between CSCM and the Winfrith model is its ability to model strain softening and modulus reduction in compression. A failure criterion in the form of maximum principal strain (MXEPS) was artificially included by defining MAT_ADD_EROSION keyword in OOPV analysis. MXEPS was calculated using Equation 8 as reported by Yang (2015), where V_e is the volume of one solid element. For IPV numerical models, element erosion was not activated due to the cyclic nature of loading protocol for actual test specimens.

$$\text{MXEPS} = \frac{\omega}{\sqrt[3]{V_e}} \tag{8}$$

The Piecewise_Linear_Plasticity (MAT 24) material model was used to simulate SC wall faceplates, connection region tie plates, wing plates, baseplates, and RC wall reinforcement. It provides the flexibility of explicitly modeling the post-yield behavior in the form of effective stress–plastic strain input curves obtained from uniaxial tensile coupon tests performed during specimen testing. SC wall

shear connectors and tie bars were modeled with a plastic kinematic (MAT 03) material model. Due to the quasi-static nature of these tests, the strain rate effects were not activated in either of these steel material models. Table 3 provides the concrete and steel material properties used in the numerical analyses. The input compressive and tensile strengths were based on the average values obtained from the material tests performed on respective test days.

Numerical Results and Discussion

Figure 38 shows the applied shear–displacement response of the numerical model compared with the experimentally observed behavior (OOPV-C test specimen). The displacement is the numerically predicted displacement under loading point. As shown, the numerical model predicts a somewhat soft response. The reason is attributed to the inherent behavior of the CSCM concrete material model. This material model is an isotropic damage model opposed to anisotropic behavior of concrete in a shear (biaxial) stress state where the compression strut can continue to carry compressive stress after tensile cracking in the orthogonal direction. Nevertheless, the numerical results are in favorable agreement with the observed behavior. The maximum shear, $V_{max}FEA$, predicted by the model is 191 kips, which is greater than the RC shear capacity ($V_{n.RC}$ = 167 kips) calculated using ACI 349-06 by 24 kips. $V_{max}FEA$ is in favorable agreement with $V_{n.RC}$. Additionally, the maximum stress predicted in the bottom layer of #14 rebar is approximately 94 ksi, which also confirms the assumption made using the mechanical connection design philosophy that the maximum axial force that needs to be transferred to the SC wall is 125% of the yield strength of the reinforcing bars

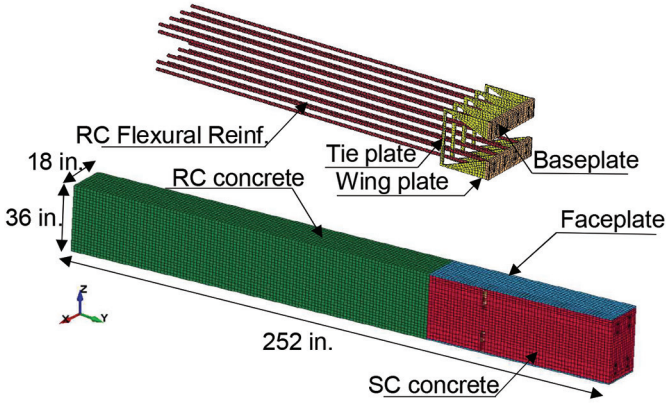

(a) Solid elements

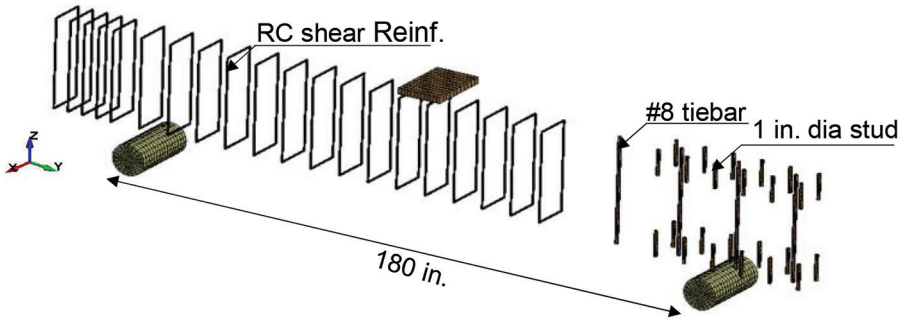

(b) Beam elements

Fig. 36. FEM element formulations (OOPV).

Table 3. Input Parameters for LS-DYNA Material Models			
Material Type	**Input Parameters**	**Value / Equation**	**Reference**
Concrete	Mass density	2.25×10^{-4} lbf s^2/in.^{4}	
	Unconfined compression strength	Table 2	Based on material tests
	Maximum aggregate size	0.75 in. (OOPV), 0.375 in. (IPV)	Experimental data
	Erosion criteria: *MXEPS*	0.005	$\text{MXEPS} = \frac{\omega}{\sqrt[3]{V_e}}$ Equation 8
Steel	Mass density	7.34×10^{-4} lbf s^2/in.^{4}	
	Young's modulus	2.9×10^7 psi	
	Poisson's ratio	0.3	
	Yield strength	Table 2	Based on material tests
	Failure strain		Based on material tests
	Hardening variable	0	LS-DYNA, 2012a, 2012b

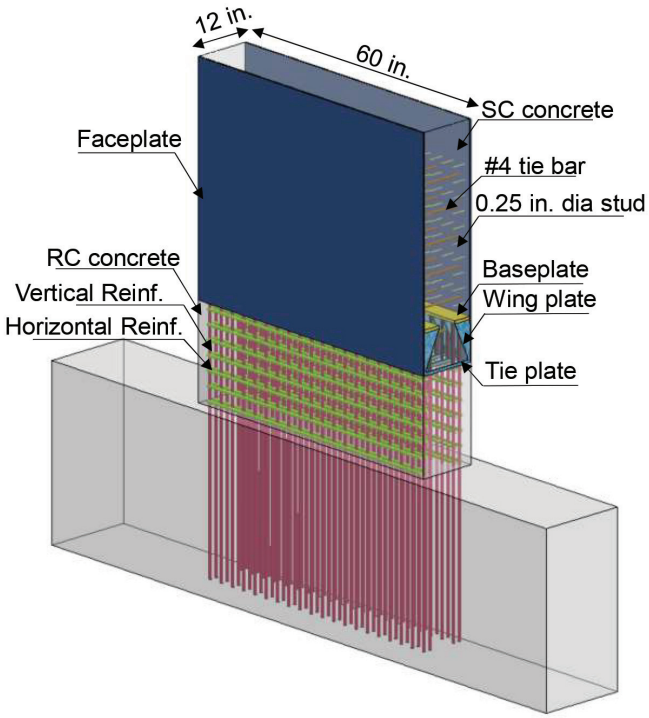

Fig. 37. LS-DYNA model (IPV).

($1.25F_{y,r}$ = 85 ksi). Strain contour plots of the mechanical connection region are shown in Figure 39. As presented, all steel components (including tie plate, wing plate, and baseplate) in the connection region remained in the elastic range until the connected RC wall portion failed in shear. Additionally, wing and baseplates were subjected to lower strain as compared to tieplates due to a significant concrete contribution, similar to what was observed during experimental verification.

Figure 40 shows the applied shear–displacement response of the numerical model compared with the experimentally measured response of the IPV-C test specimen. The displacement is the numerically predicted value at the loading point (60 in. from the base of RC wall). The model underwent a series of events such as vertical rebar yielding, tie bar yielding, and stud yielding (not shown here for brevity). The analysis was eventually stopped due to unstable shear failure of the RC wall portion after exceeding its shear capacity ($V_{n.RC}$ = 554 kips). The maximum shear force predicted from the model, V_{maxFEA}, is 564 kips. V_{maxFEA} is in favorable agreement with $V_{n.RC}$ within an accuracy of 2%. Longitudinal strain contour plots of the mechanical connection region are shown in Figure 41. The maximum respective strain values in tie plates, wing plates, and baseplates at V_{maxFEA} indicate that all steel components in the connection region remained in the elastic range and the wing and baseplates were subjected to lower strain as compared to the tieplates. The predicted strain values for both OOPV and IPV models were lower than the experimentally observed response. This is attributed to the treatment of the connection region in the numerical models. The connection region was embedded inside the infill concrete in

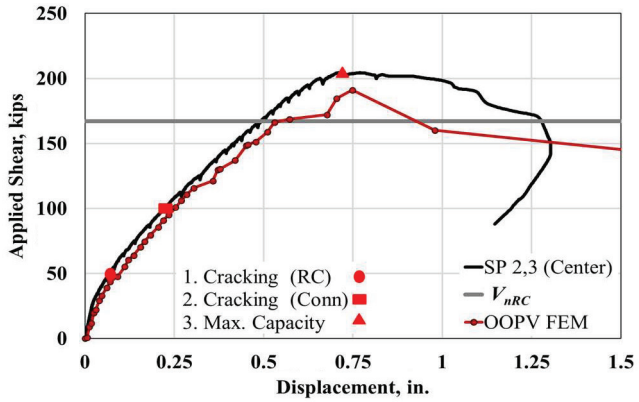

Fig. 38. Comparison between experimental (OOPV-C) and FEA results.

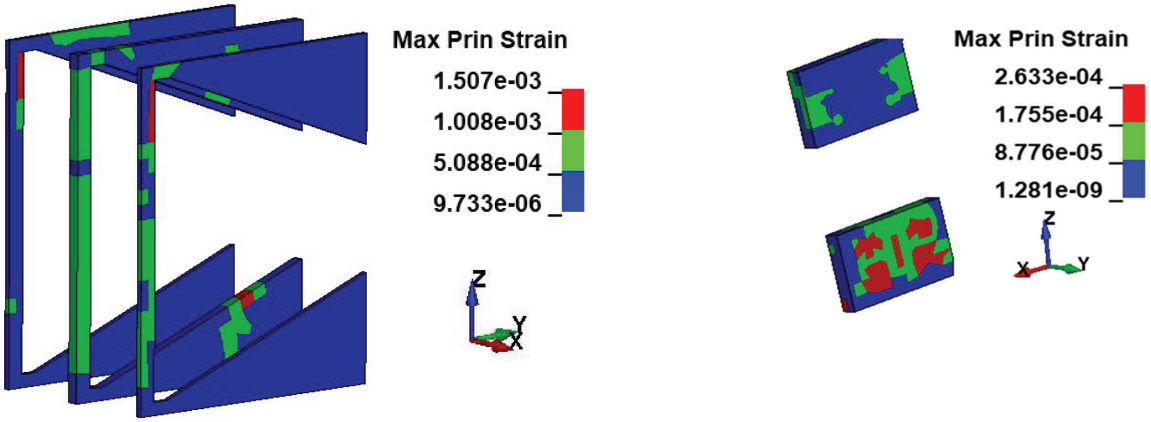

(a) Tie plate and wing plate *(b) Baseplate*

Fig. 39. OOPV strain contour plot.

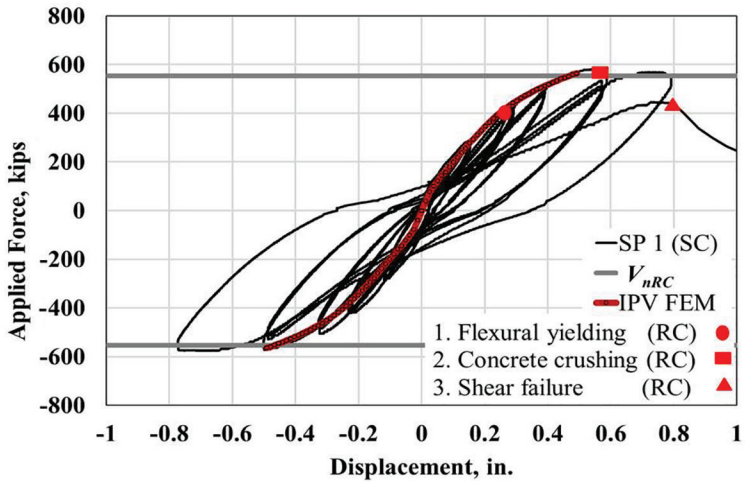

Fig. 40. Comparison between experimental (IPV-C) and FEA results.

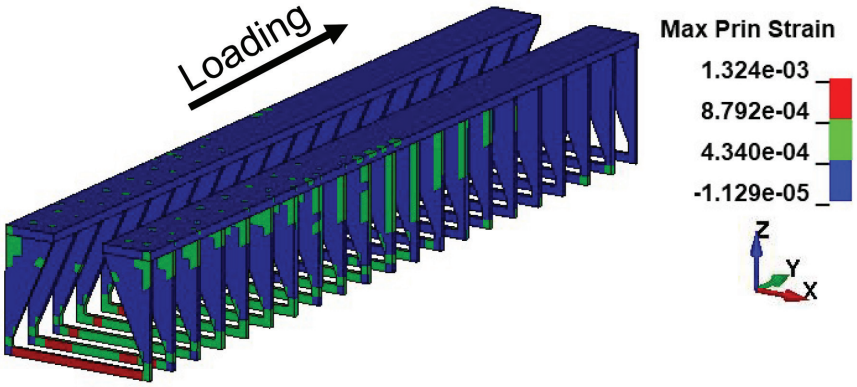

Fig. 41. Connection region strain contour plot (IPV).

Table 4. Summary of Test Results						
Specimen	Maximum Load ^{Exp}, P_{max}, V_{max} (kips)	Maximum Load ^{FEA}, P_{max}^{FEA}, V_{max}^{FEA} (kips)	RC Capacity, P_{MnRC}, V_{nRC} (kips)	Max. Load^{Exp} RC Capacity	Max. Load^{FEA} RC Capacity	Failure Mode
OOPM-C	585	571	495	1.18	1.15	RC flexural yielding
OOPM-DN	571		494	1.15		RC flexural yielding
OOPV-C	205	191	167	1.23	1.14	RC shear
OOPV-DN	189		167	1.13		RC shear
IPV-C	579	564	554	1.04	1.02	RC shear
IPV-DN	566		531	1.06		RC shear

Table 5. Comparison Between Maximum Steel Strain and Stress Values							
		Maximum Microstrain (in./in. × 10^{-6})			Maximum Stress (ksi)		
Verification	Specimen	Tie plate	Wing plate	Baseplate	Tie plate	Wing plate	Baseplate
Experimental	OOPM-C	1436	360	802	42	10	23
	OOPM-DN	1671	297	176	49	9	5
	OOPV-C	1370	60	436	40	2	13
	OOPV-DN	1012	100	245	29	3	7
	IPV-C	1932	365	–	56	11	–
	IPV-DN	2193	–	–	64	–	–
Numerical	OOPM	1600	313	120	46	9	4
	OOPV	855	194	147	25	6	4
	IPV	1280	131	–	37	4	–

the models depicting a perfect bond, whereas limited bonding was achieved in the test specimens. Nevertheless, the predicted response is in reasonable agreement with the observed behavior.

SUMMARY AND CONCLUSIONS

This section presents the important findings and conclusions from the complete study including both Part 1 (Seo et al., 2022) and Part 2 of this series of papers. The study aimed at the development and validation (both experimental and numerical) of the performance, strength, ductility, and failure modes of the designed mechanical connection. The designed connection was based on a full-strength connection design philosophy. The experimental program involved testing seven mechanical connections comprised of four full-scale and three scaled specimens. Full-scale specimens were subjected to monotonic out-of-plane moment (OOPM) and out-of-plane shear (OOPV). The remaining three scaled specimens were subjected to cyclic in-plane shear (IPV). The two rebar-to-baseplate connection configurations—coupler (C) and double nut (DN)—were tested. The observed applied force–displacement and applied force–steel strain responses were evaluated to determine the ultimate strength and governing failure modes. Additionally, detailed finite element models (FEMs) were developed and benchmarked against experimental data to gain an additional insight into the connection behavior and to compensate for the limited experimental database.

Table 4 summarizes the results from the experimental and numerical investigation. As presented, the observed and predicted governing failure mode of all test specimens is either RC flexural yielding or RC shear failure. The experimentally observed maximum loads, P_{max} and V_{max}, of all test specimens exceeded their respective RC capacities, $P_{Mn.RC}$ and $V_{n.RC}$. In addition, the predicted maximum loads, P_{max}^{FEA} and V_{max}^{FEA}, of all three numerical models are greater than the respective RC capacities, $P_{Mn.RC}$ and $V_{n.RC}$,

and are in reasonable agreement with the observed values. Table 5 presents a summary of maximum strain and the corresponding stress values of the steel components in the connection region from both experimental and numerical verification. As shown, all steel components (including tieplates, wing plates, and baseplates) in the connection region remained in the elastic range, except the tieplates of Specimen IPV-DN, until the connected RC wall portion developed its capacity (either RC flexural yielding or RC shear). For Specimen IPV-C and IPV-DN relatively higher tie plate strain values are attributed to the location of gauges on the test specimens, i.e., strain gauges were installed on the two exterior tieplates (3⁄16 in.) which were thinner than the interior tieplates (3⁄8 in.) by 50%.

The results from both experimental and numerical investigations concluded that:

(1) SC wall-to-RC wall mechanical connections should be designed and detailed to develop the full-strength of the weaker of the two connected structures in order to ensure energy dissipation away from the connection region during a design level earthquake.

(2) The type of rebar-to-baseplate connection configuration, coupler (C) or double nut (DN), does not have a significant influence on the force transfer mechanism of the designed connection.

(3) Tieplates connecting the two opposite faceplates are recommended in the connection region to resist the tensile component of the moment generated due to the eccentricity associated with force transfer from rebar to faceplates.

(4) Due to rebar congestion caused by a high steel reinforcement ratio, caution is required in cases with cast-in-place concrete near the connection region and RC wall portion to prevent honey combing, voids, and premature failure. Self-consolidating concrete is recommended under such situations.

(5) All the steel components in the connection region including tie plates, wing plates, and baseplates remained in the elastic range until the RC wall developed its flexural or shear capacity.

(6) Experimentally observed and numerically predicted strain values in the wing plates and baseplates remained below their respective yield strains. This is attributed to the significant contribution of concrete during the force transfer from RC-to-SC structure exhibiting conservatism in the designed mechanical connection.

(7) The proposed connection design procedure is suitable and conservative for SC wall-to-RC wall mechanical connections.

(8) Additional experimental and numerical studies are recommended to further expand the limited database, and to evaluate the influence of different design parameters including wall thickness, rebar layers, rebar-to-baseplate connection, and tie plate configuration, etc.

ACKNOWLEDGEMENTS

The authors would like to acknowledge the valuable contribution of KEPCO E&C, Korea, (sponsor) and all the technical staff involved in the experimental and numerical work during the execution of the project. However, the views presented in this paper are solely that of the authors.

REFERENCES

ACI (2006), *Code Requirements for Nuclear Safety-Related Concrete Structures (ACI 349-06) and Commentary*, ACI 349-06, American Concrete Institute, Farmington Hills, Mich.

ACI (2019), *Building Code Requirements for Structural Concrete*, ACI 318-19, American Concrete Institute, Farmington Hills, Mich.

AISC (2015), *Specification for Safety-Related Steel Structures for Nuclear Facilities Including Supplement No. 1*, ANSI/AISC N690s1-15, American Institute of Steel Construction, Chicago, Ill.

AISC (2018), *Specification for Safety-Related Steel Structures for Nuclear Facilities*, ANSI/AISC N690-18, American Institute of Steel Construction, Chicago, Ill.

AISC (2019), *Companion to the AISC Steel Construction Manual Volume 1: Design Examples*, Version 15.1, American Institute of Steel Construction, Chicago, Ill.

ASTM (2013), *Standard Test Method for Tension Testing of Metallic Materials*, ASTM E8/E8M, ASTM International, West Conshohocken, Pa.

ASTM (2014), *Standard Test Method for Compressive Strength of Cylindrical Concrete Specimens*, ASTM C39/C39M, ASTM International, West Conshohocken, Pa.

Anvari, A. T., Bhardwaj, S.R., Wazalwar, P., and Varma, A.H. (2020), "Stability of Speedcore Walls Under Fire Loading: Summary of Numerical Analyses," *Proceedings of the Annual Stability Conference, Structural Stability Research Council*, April 21–24, Atlanta, Ga.

Bhardwaj, S.R. and Varma, A.H. (2017), *Design of Modular Steel-Plate Composite Walls for Safety Related Nuclear Facilities*, Design Guide 32, AISC, Chicago, Ill.

Biskinis, D.E., Roupakias, G.K., and Fardis, M.N. (2004), "Degradation of Shear Strength of Reinforced Concrete Members with Inelastic Cyclic Displacements," *ACI Structural Journal*, Vol. 101, Issue 6, pp. 773–783.

Booth, P.N., Bhardwaj, S.R., Tseng, T.C., Seo, J., and Varma, A.H. (2020), "Ultimate Shear Strength of Steel-Plate Composite (SC) Walls with Boundary Elements," *Journal of Constructional Steel Research*, Vol. 165. https://doi.org/10.1016/j.jcsr.2019.105810

Bruhl, J., Varma, A.H., and Johnson, W.H. (2015a), "Design of Composite SC Walls to Prevent Perforation from Missile Impact," *International Journal of Impact Engineering*, Vol. 75, pp. 75–87. http://dx.doi.org/10.1016/j.ijimpeng.2014.07.015

Bruhl, J.C., Varma, A.H., and Kim, J.M. (2015b), "Static Resistance Function for Steel-Plate Composite (SC) Walls Subject to Impactive Loading," *Nuclear Engineering and Design,* Vol. 295, pp. 843–859. https://doi.10.1016/j.nucengdes.2015.07.037

Carrillo, J. and Alcocer, S.M. (2013), "Shear Strength of Reinforced Concrete Walls for Seismic Design of Low-Rise Housing," *ACI Structural Journal*, Vol. 110, Issue 3.

DOE (2006), "Accident Analysis for Aircraft Crash into Hazardous Facilities," DOE-STD-3014, U.S. Department of Energy, Washington, D.C.

Epackachi, S., Nguyen, N.H., Kurt, E.G., Whittaker, A.S., and Varma, A.H. (2015a), "In-Plane Seismic Behavior of Rectangular Steel-Plate Composite Wall Piers," *Journal of Structural Engineering*, Vol. 141, Issue 7. http://dx.doi.10.1061/(ASCE)st.1943-541x.0001148

Epackachi, S., Whittaker, A.S., Varma, A.H., and Kurt, E.G. (2015b), "Finite Element Modeling of Steel-plate Concrete Composite Wall Piers," *Engineering Structures*, Vol. 100, pp. 369–384.

Hwang, K.M., Lee, K.J., and Kim, W.K. (2013), "An Experimental Study on the Flexural and Shear Behavior of Steel Plate Concrete—Reinforced Concrete Connected Structures," *Nuclear Engineering and Design*, Vol. 257, pp. 88–99. https:// dx.doi.org/10.1016/j.nucengdes.2012.12.020

IAEA (2011), "Construction Technologies for Nuclear Power Plants," IAEA Nuclear Energy Series No. NP-T-2.5, International Atomic Energy Agency, Vienna.

JEAC (2009), *Technical Code for Seismic Design of Steel Plate Reinforced Concrete Structures: Buildings and Structures*, JEAC-4618, Japanese Electric Association Nuclear Standards Committee, Tokyo, Japan.

Kurt, E.G. (2016), "Steel-Plate Composite (SC) Walls and their Basemat Connections: Seismic Behavior, Analysis, and Design," Ph.D. Dissertation, Purdue University, West Lafayette, Ind.

LS-DYNA (2012a), Keyword User's Manual, Volume I, Version 971 R6.0.0, Livermore Software Technology Corporation (LSTC), Livermore, Calif.

LS-DYNA (2012b), Keyword User's Manual, Volume II, Version 971 R6.0.0, Livermore Software Technology Corporation (LSTC), Livermore, Calif.

Mo, Y.L., Zhong, J., and Hsu, T.C. (2008), "Seismic Simulation of RC Wall-Type Structures," *Engineering Structures*, Vol. 30, Issue 11, pp. 3,2167–3,175.

Ottosen, N.S. (1977), "A Failure Criterion for Concrete," *Journal of Engineering Mechanics Division*, Vol. 103, No. 4, pp. 527–535.

Ozaki, M., Akita, S., Osuga, H., Nakayama, T., and Adachi, N. (2004), "Study on Steel Plate Reinforced Concrete Panels Subjected to Cyclic In-Plane Shear," *Nuclear Engineering and Design*, Vol. 228, pp. 225–244. https://doi.org/10.1016/j.nucengdes.2003.06.010

Schwer, L. (2011). "The Winfrith Model: Beauty or Beast? Insights into the Winfrith Concrete Model," *Proceedings of the 8th European LS-DYNA Users Conference*, Strasbourg.

Sener, K., Varma, A.H., Booth, P.N., and Fujimoto, R. (2015), "Seismic Behavior of a Containment Internal Structure Consisting of Composite SC Walls," *Nuclear Engineering and Design*, Vol. 295, pp. 804–816. http://dx.doi.org/10.1016/j.nucengdes.2015.07.038

Sener, K.C., and Varma, A.H. (2021), "Steel-Plate Composite Walls with Different Types of Out-of-Plane Shear Reinforcement: Behavior, Analysis, and Design," *Journal of Structural Engineering*, Vol. 147, Issue 2. https://doi.10.1061/(ASCE)st.1943-541x.0002870

Seo, J., Varma, A.H., Sener, K., and Ayhan, D. (2016), "Steel-Plate Composite (SC) Walls: In-Plane Shear Behavior, Database, and Design," *Journal of Constructional Steel Research*, Vol. 119, pp. 202–215. https://doi.org/10.1016/j.jcsr.2015.12.013

Seo, J. and Varma, A.H. (2017a), "Experimental Behavior and Design of Steel Plate Composite-to-Reinforced Concrete Lap Splice Connections," *Journal of Structural Engineering*, Vol. 143, Issue 5. https://doi. 10.1061/(ASCE)st.1943-541x.0001711

Seo, J. and Varma, A.H. (2017b), "SC Wall-to-Slab Connections in Safety Related Nuclear Facilities," *Proceedings of the 24th International Conference on Structural Mechanics in Reactor Technology (SMiRT-24)*, August 20–25, Busan, Korea.

Seo, J., Anwar, H.S., and Varma, A.H. (2022), "Steel-Plate Composite (SC) Wall-to-Reinforced Concrete (RC) Wall Mechanical Connection- Part 1," *Engineering Journal*, AISC, Vol. 59, No.1, pp. 31–52.

Teh Hu, H. and Schnobrich, W.C. (1990), "Nonlinear Analysis of Cracked Reinforced Concrete," *ACI Structural Journal*, Vol. 87, No. 2, pp. 199–207.

Usta, M. (2017), "Shear Strength of Structural Walls Subjected to Load Cycles," Ph.D. Dissertation, Purdue University, West Lafayette, Ind.

Varma, A.H., Malushte, S.R., Sener, K.C., and Lai, Z. (2014), "Steel-Plate Composite (SC) Walls for Safety Related Nuclear Facilities: Design for In-Plane Forces and Out-of-Plane Moments," *Nuclear Engineering and Design*, Vol. 269, pp. 240–249. https://dx.doi.org/10.1016/j.nucengdes.2013.09.019

Vecchio, F.J. and DeRoo, A. (1995), "Smeared-Crack Modeling of Concrete Tension Splitting," *Journal of Engineering Mechanics*, Vol. 121, No. 6.

Wittmann, F.H., Rokugo, K., Bruhwiler, E., Mihashi, H., and Simonin, P. (1988), "Fracture Energy and Strain Softening of Concrete as Determined by Means of Compact Tension Specimens," *Materials and Structures*, Vol. 21, Issue 121, pp. 21–32.

Yang, Y. (2015), "Shear Strength and Behavior of Reinforced Concrete Structures with T-Headed Bars in Safety-Related Nuclear Facilities," Ph.D. Dissertation, Purdue University, West Lafayette, Ind.